Front. Phys., 2013, 8(3): 302–318
DOI 10.1007/s11467-013-0350-8

REVIEW ARTICLE

Ground states, solitons and spin textures in spin-1 Bose–Einstein condensates

Shu-Wei Song[1], **Lin Wen**[1], **Chao-Fei Liu**[2], **S.-C. Gou**[3], **Wu-Ming Liu**[1,†]

[1] *Beijing National Laboratory for Condensed Matter Physics, Institute of Physics, Chinese Academy of Sciences, Beijing 100190, China*

[2] *School of Science, Jiangxi University of Science and Technology, Ganzhou 341000, China*

[3] *Department of Physics, National Changhua University of Education, Changhua 50058, Taiwan, China*

E-mail: [†] *wmliu@aphy.iphy.ac.cn*

Received February 24, 2013; accepted May 22, 2013

We present an overview of our recent theoretical studies on the quantum phenomena of the spin-1 Bose–Einstein condensates, including the phase diagram, soliton solutions and the formation of the topological spin textures. A brief exploration of the effects of spin–orbit coupling on the ground-state properties is given. We put forward proposals by using the transmission spectra of an optical cavity to probe the quantum ground states: the ferromagnetic and polar phases. Quasi-one-dimension solitons and ring dark solitons are studied. It is predicted that characteristics of the magnetic solitons in optical lattice can be tuned by controlling the long-range light-induced and static magnetic dipole-dipole interactions; solutions of single-component magnetic and single-, two-, three-components polar solitons are found; ring dark solitons in spin-1 condensates are predicted to live longer lifetimes than that in their scalar counterparts. In the formation of spin textures, we have considered the theoretical model of a rapidly quenched and fast rotating trapped spin-1 Bose–Einstein condensate, whose dynamics can be studied by solving the stochastic projected Gross–Pitaevskii equations. Spontaneous generation of nontrivial topological defects, such as the hexagonal lattice skyrmions and square lattice of half-quantized vortices was predicted. In particular, crystallization of merons (half skyrmions) can be generated in the presence of spin–orbit coupling.

Keywords Bose–Einstein condensate, spinor, vortex lattice, soliton, spin–orbit coupling

PACS numbers 03.75.Lm, 03.75.Mn, 67.85.-d, 03.75.Kk

Contents

1 Introduction

Since the experimental realization of Bose–Einstein condensates (BECs), intensive interest in this field has been growing and the condensate has been an ideal platform for various effects of quantum many-body interaction. This opens a new field to explore various types of excitations. BECs in optical traps liberate the spin degrees of freedom of the atoms and distinguish themselves from their scalar counterparts by their much richer internal structures and dynamics [1–4]. Thus, the ultra-cold atomic gas is composed of atoms in components with different magnetic quantum numbers and such a conden-

sate is referred to as a spinor condensate. In addition, BECs have a high degree of experimental manipulability. Thus spinor BEC is identified as unique playground for exploring quantum phenomena related to the symmetry breaking, topological excitations, and the interplay between superfluidity and magnetism. Based on the single mode approximation, the quantum eigenstates of a spinor BEC have been extensively studied with sophisticated algebraic techniques [5–7]. A rich variety of phenomena, such as spin domains [8] and textures [2] and spin-mixing [9] arise in the condensate held by an optical potential.

At zero external magnetic field, the ground state of the spin-1 condensate is determined by the spin-dependent interaction term in the Hamiltonian [4, 10–12]. Vortices excitations have been extensively explored, such as fractional vortices [13–15], coreless vortices [3, 16–19], and Monopoles [20, 21]. Soliton dynamics and Bright-dark soliton complexes are investigated in Refs. [22–24], and the existence of multiple bright solitons was shown by proving that the system possesses a completely integrable point.

In this article, we review our recent theoretical advances in the stationary and dynamical characteristics of the spin-1 BECs. In Section 2, we derive the mean field Hamiltonian and equations from the second quantized form of the Hamiltonian to describe the stationary and dynamic characteristics of the spin-1 condensate. Section 3 is devoted to investigating the ground states of the spin-1 condensates with external parabolic potential and proposals to distinguish experimentally the ferromagnetic and polar phases of the condensate. We show the soliton solutions and dynamics of one or two dimensional spin-1 BECs in Section 4. Section 5 focuses on the nontrivial topological structure: skyrmion lattices. Finally, we summarize our results in Section 6.

2 Derivation of the mean-field model

In cold atomic vapours, particle separations are usually an order of magnitude larger than the length scales associated with the atom–atom interaction. Thus, we can approximately take account of the binary collisions between atoms. In addition, because the ultra-cold atoms have low velocities, only the s-wave scattering length a_s is necessary to describe the interaction characteristics of the colliding atoms.

The single-particle Hamiltonian of the spin-1 atoms in the second quantized form is [25]

$$\hat{H}_0 = \int \mathrm{d}\boldsymbol{r} \sum_{k,l=-1}^{1} \hat{\psi}_k^{\dagger}\Big(-\frac{\hbar^2\nabla^2}{2M} + U(\boldsymbol{r}) - p(F_z)_{kl} + q(F_z^2)_{kl}\Big)\hat{\psi}_l \tag{1}$$

where $\hat{\psi}_k$ is the field operator with $k = 0, \pm 1$ denoting the magnetic quantum number and M is the mass of the atom. F_z is the z-component of the spin matrix and $U(\boldsymbol{r})$ is the one-body potential. The coefficient in the linear Zeeman term is $p = -g\mu_B B$, where g, μ_B and B are the landé hyperfine g factor, Bohr magneton and magnetic field that is assumed to be applied in the z-direction, respectively. In the quadratic Zeeman term, $q = (g\mu_B B)^2/(E_k - E_i)$, where E_i and E_k are the initial and the intermediate energies, respectively. In the following, we focus on the derivation of the interaction part of the Hamiltonian in the second quantized form.

Exchange symmetry states that the many-body wave function does not change upon the exchange of two identical particles for bosons. Since only the s-wave scattering is considered, the orbital part of the wave function does not change under this exchange of two identical particles, indicating that confinements need to be exerted on the spin part of the many-body wave function, i.e., the total spin of two interacting particles must be even. To understand this issue more clearly, we can recall the spin part of the binary wave function for spin-1 atoms.

Considering two colliding atoms whose spin operators are denoted by $\hat{\boldsymbol{F}}_1$ and $\hat{\boldsymbol{F}}_2$, the total spin operator is

$$\hat{\boldsymbol{F}} = \hat{\boldsymbol{F}}_1 + \hat{\boldsymbol{F}}_2 \tag{2}$$

We denote the simultaneous eigenstates of $\hat{\boldsymbol{F}}_1^2$, $\hat{\boldsymbol{F}}_2^2$, $\hat{\boldsymbol{F}}_{1z}$ and $\hat{\boldsymbol{F}}_{2z}$ by $|f_1, m_1; f_2, m_2\rangle$ $(m_1, m_2 = 1, 0, -1)$, which satisfy

$$\begin{aligned}
&\hat{\boldsymbol{F}}_1^2|f_1, m_1; f_2, m_2\rangle = 2\hbar^2|f_1, m_1; f_2, m_2\rangle\\
&\hat{\boldsymbol{F}}_2^2|f_1, m_1; f_2, m_2\rangle = 2\hbar^2|f_1, m_1; f_2, m_2\rangle\\
&\hat{\boldsymbol{F}}_{1z}|f_1, m_1; f_2, m_2\rangle = m_1\hbar|f_1, m_1; f_2, m_2\rangle\\
&\hat{\boldsymbol{F}}_{2z}|f_1, m_1; f_2, m_2\rangle = m_2\hbar|f_1, m_1; f_2, m_2\rangle
\end{aligned} \tag{3}$$

The simultaneous eigenstates of $\hat{\boldsymbol{F}}^2$ and $\hat{\boldsymbol{F}}_1^2$, $\hat{\boldsymbol{F}}_2^2$ and F_z are $|f_1, f_2; f, m\rangle$ $(f = |f_1 - f_2|, \cdots, f_1 + f_2 - 1, f_1 + f_2$ and $m = -f, -f + 1, \cdots, f)$, which satisfy

$$\begin{aligned}
&\hat{\boldsymbol{F}}_1^2|f_1, f_2; f, m\rangle = 2\hbar^2|f_1, f_2; f, m\rangle\\
&\hat{\boldsymbol{F}}_2^2|f_1, f_2; f, m\rangle = 2\hbar^2|f_1, f_2; f, m\rangle\\
&\hat{\boldsymbol{F}}^2|f_1, f_2; f, m\rangle = f(f+1)\hbar^2|f_1, f_2; f, m\rangle\\
&\hat{\boldsymbol{F}}_z|f_1, f_2; f, m\rangle = m\hbar|f_1, f_2; f, m\rangle
\end{aligned} \tag{4}$$

The Clebsch–Gordan coefficients connect these two set of eigenstates. Here for spin-1 atoms, $f = 0, 1, 2$. However, the $f = 1$ states change sign upon the exchange of two identical atoms. Actually, for $f = 1$, the three states with magnetic number $m = 1, 0, -1$ are

$$|f_1, f_2; 1, 1\rangle = \frac{1}{\sqrt{2}}\left[|f_1, 1; f_2, 0\rangle - |f_1, 0; f_2, 1\rangle\right]$$

$$|f_1,f_2;1,0\rangle = \frac{1}{\sqrt{2}}\left[|f_1,1;f_2,-1\rangle - |f_1,-1;f_2,1\rangle\right]$$
$$|f_1,f_2;1,-1\rangle = \frac{1}{\sqrt{2}}\left[|f_1,0;f_2,-1\rangle - |f_1,-1;f_2,0\rangle\right] \quad (5)$$

Thus, the total spin of two interacting particles must be even, i.e., $f = 0, 2$. Consequently, there are two scattering lengths a_0 and a_2 to describe the scattering characteristics corresponding to these two channels of total spin $f = 0, 2$. Following Ref. [3], the form of the interaction can be written as

$$\hat{V}_{int} = 4\pi\hbar^2/M\delta(\boldsymbol{r}_1 - \boldsymbol{r}_2)\left(a_0\mathcal{P}_0 + a_2\mathcal{P}_2\right) \quad (6)$$

where, $\mathcal{P}_0$ and $\mathcal{P}_2$ are the projection operators which project the binary interaction into two channels of total spin $f = 0, 2$, respectively. Next, we need to find ways to express the projection operators. Fortunately, we have the composition law as

$$\boldsymbol{F}^2 = (\boldsymbol{F}_1 + \boldsymbol{F}_2)^2 \quad (7)$$

Thus, we have

$$\boldsymbol{F}_1 \cdot \boldsymbol{F}_2 = \begin{cases} -2 & f = 0 \\ 1 & f = 2 \end{cases} \quad (8)$$

Then we can express $\boldsymbol{F}_1 \cdot \boldsymbol{F}_2$ in terms of the projection operators like

$$\boldsymbol{F}_1 \cdot \boldsymbol{F}_2 = -2\mathcal{P}_0 + \mathcal{P}_2 \quad (9)$$

On the other hand, by referring to the completeness of the projection operators $\mathcal{P}_0 + \mathcal{P}_2 = 1$, we finally obtain

$$\mathcal{P}_0 = \left(1 - \boldsymbol{F}_1 \cdot \boldsymbol{F}_2\right)/3$$
$$\mathcal{P}_2 = \left(2 + \boldsymbol{F}_1 \cdot \boldsymbol{F}_2\right)/3 \quad (10)$$

After the substitution of Eq. (10) into Eq. (6), we have

$$\hat{V}_{int} = \delta(\boldsymbol{r}_1 - \boldsymbol{r}_2)\left(g_n + g_s\boldsymbol{F}_1 \cdot \boldsymbol{F}_2\right) \quad (11)$$

where $g_n = 4\pi\hbar^2(a_0 + 2a_2)/(3M)$, $g_s = 4\pi\hbar^2(a_2 - a_0)/(3M)$. Then we obtain the interaction part of the total Hamiltonian in the second quantized form

$$H_{int} = \int \mathrm{d}\boldsymbol{r}\frac{1}{2}(g_n\hat{\psi}_k^\dagger\hat{\psi}_{k'}^\dagger\hat{\psi}_{k'}\hat{\psi}_k + g_s\hat{\psi}_k^\dagger\hat{\psi}_{k'}^\dagger\boldsymbol{F}_{kl}\cdot\boldsymbol{F}_{k'l'}\hat{\psi}_{l'}\hat{\psi}_l) \quad (12)$$

where $\boldsymbol{F} = (F_x, F_y, F_z)$ ($F_{x,y,z}$ are the spin-1 matrices). In the interaction part of the Hamiltonian, the Einstein summation convention is used ($k, k' = 1, 0, -1$).

In the mean-field approximation, the Bose–Einstein condensate wavefunction $\psi_k = \langle\hat{\psi}_k\rangle$. Thus, the mean-field Hamiltonian of the spin-1 Bose–Einstein condensate is

$$H = \int \mathrm{d}\boldsymbol{r}\left[\psi_k^*\left(-\frac{\hbar^2\nabla^2}{2M} + U(\boldsymbol{r}) - p(F_z)_{kl} + q(F_z^2)_{kl}\right)\psi_l + \frac{1}{2}(g_n\psi_k^*\psi_{k'}^*\psi_{k'}\psi_k + g_s\psi_k^*\psi_{k'}^*\boldsymbol{F}_{kl}\cdot\boldsymbol{F}_{k'l'}\psi_{l'}\psi_l)\right] \quad (13)$$

In the following sections, the time-splitting spectral method [26] is used to solve the coupled nonlinear Gross–Pitaevskii equations at zero temperature. For dynamics of the condensate at finite temperature, we solve the stochastic projected Gross–Pitaevskii equations [27–33].

3 Ground states

3.1 Ground states of the trapped condensate

The density distribution of one dimension spin-1 bosonic condensate in its ground state can be evaluated within a modified Gross–Pitaevskii theory and obvious Fermi-like distribution emerges for each component [34]. In this section we focus on pancake BECs composed of ^{23}Na and ^{87}Rb atoms. As pointed out in Refs. [3, 4], the ground state can be a polar or ferromagnetic state according to the spin-dependent interaction term $g_s\psi_k^*\psi_{k'}^*\boldsymbol{F}_{kl}\cdot\boldsymbol{F}_{k'l'}\psi_{l'}\psi_l/2$. The polar state will be realized with $g_s > 0$, and the ferromagnetic state with $g_s < 0$.

Following the interaction parameters in Ref. [3], we choose $a_0 = 46a_B$, $a_2 = 52a_B$ (a_B is the Bohr radius) for ^{23}Na condensate and $a_0 = 110a_B$, $a_2 = 107a_B$ for ^{87}Rb condensate. Thus, the ground state is polar for the ^{23}Na condensate and ferromagnetic for the ^{87}Rb condensate. In Fig. 1, we show the quasi-two-dimension density distribution with a total atom number $N = 1 \times 10^4$.

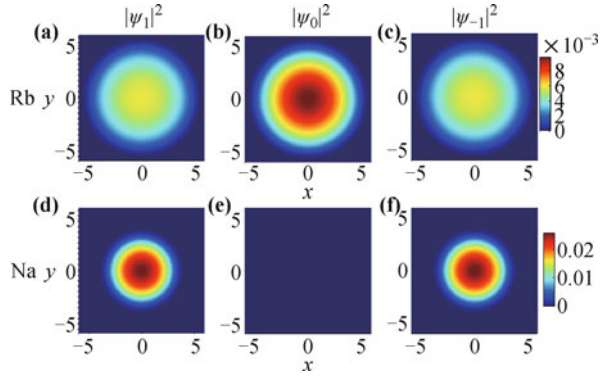

Fig. 1 The three components density distributions for spinor ^{87}Rb condensate **(a)**–**(c)** and ^{23}Na condensate **(d)**–**(f)**. The total atom number is $N_{\mathrm{Rb}} = N_{\mathrm{Na}} = 1\times10^4$. The length, time and energy are respectively scaled in units of $a_\perp = \sqrt{\hbar/(M\omega_\perp)}$, $\tau = 1/\omega_\perp$ and $\hbar\omega_\perp$. $\omega_\perp = \omega_x = \omega_y = (2\pi) \times 12$ Hz and $\omega_z = (2\pi) \times 372$ Hz, respectively ($\omega_{x,y,z}$ is the confinement frequency in the corresponding direction).

In fact, all spinors are related to each other by gauge transformation $\mathrm{e}^{\mathrm{i}\theta}$ and spin rotations $R(\alpha, \beta, \gamma)$ (α, β, γ are Euler angles), and all of them are degenerate. Thus the density configuration shown in Fig. 1 is not unique.

Corresponding to the density distribution of the ^{87}Rb condensate, Fig. 2 shows the ferromagnetic spin structure, showing the spin magnetic moments align along x direction.

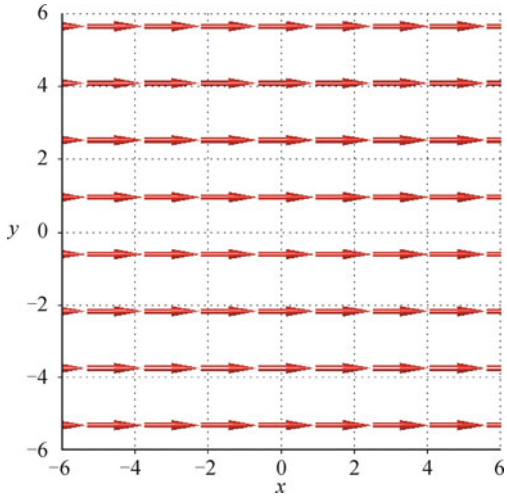

Fig. 2 The spin structure in the ground state of the spin-1 ^{87}Rb condensate.

As pointed out in Refs. [35–37], we should keep in mind that nonlinear modulation instability of soliton structures in the spinor BECs would occur. Spinor BEC with ferromagnetic interactions can spontaneously generates a topological spin texture [38]. Even for the ground state, the ferromagnetic phase of the condensate may experience modulational instability, leading to a fragmentation of the spin domains. The effect of the modulational instability is shown in Fig. 3 for a pancake ferromagnetic condensate.

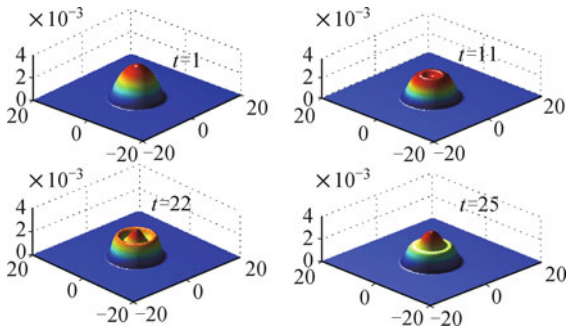

Fig. 3 Development of the modulational instability in the two dimension spinor ^{87}Rb condensate. The density profile of the spin component with magnetic quantum number $k = 1$ is shown, and the other two components behave similarly. The initial condition is the ground state obtained by imaginary time evolution. $\omega_\perp = \omega_x = \omega_y = (2\pi) \times 12$ Hz and $\omega_z = (2\pi) \times 372$ Hz, respectively ($\omega_{x,y,z}$ is the confinement frequency in the corresponding direction).

3.2 Condensate with spin–orbit coupling

The spin–orbit coupling is an essential mechanism for spintronics devices, and many fundamental phenomena in condensed matter physics and atomic physics have a firm relationship with it. For instance, spin–orbit coupling causes the appearance of the quantum spin Hall effect in electronic condensed matter systems [39]. Artificial external Abelian and non-Abelian gauge potentials coupled to neutral atoms have been generated recently by controlling the atom–light interaction [40–45], and this provides the possibility of spin control in neutral atom systems through laser fields. In the presence of the spin–orbit coupling, the neutral atoms in the effective abelian and non-abelian gauge fields behave like electrons in an electro–magnetic field. Thus, spin–orbit coupled ultra-cold atom systems have attracted intensive attention since last few years [46–63].

In the presence of the Rashba spin–orbit coupling, the Hamiltonian can be written as

$$H = \int \mathrm{d}\boldsymbol{r}\Big[\psi_k^*\Big(-\frac{\hbar^2\nabla^2}{2M} + U(\boldsymbol{r}) + \frac{\hbar\kappa}{M}(\partial_x(F_x)_{kl} + \partial_y(F_y)_{kl})\Big)\psi_l + \frac{1}{2}(g_n\psi_k^*\psi_{k'}^*\psi_{k'}\psi_k + g_s\psi_k^*\psi_{k'}^*\boldsymbol{F}_{kl}\cdot\boldsymbol{F}_{k'l'}\psi_{l'}\psi_l)\Big] \quad (14)$$

where κ characterizes the strength of the spin–orbit coupling strength, which is experimentally related to the wavelength of the laser beams and exact experimental setups. As proposed in Ref. [64], $\kappa = 2\pi\hbar\sin(\theta/2)/\lambda$, ($\theta$ and λ are the angle between two Raman beams and the wavelength of the laser, respectively.). In Ref. [65], the tetrapod setup is used to generate the Rashba spin–orbit coupled BEC and it requires $\kappa = \sqrt{2}\pi\hbar/\lambda$.

Experimentally, the quasi-two-dimension condensate can be realized by imposing a strong harmonic confinement, i.e., $\omega_z \gg \omega_\perp = \omega_x = \omega_y$. After the integral along z direction, the effective two dimensional Hamiltonian within the mean-field theory we can be expressed as

$$H = \int \mathrm{d}\boldsymbol{r}\Big\{\sum_{m=0,\pm1}\Big[-\frac{\hbar^2}{2M}\psi_m^*\nabla^2\psi_m + \frac{1}{2}M\omega_\perp^2(x^2+y^2)|\psi_m|^2\Big] + \frac{\hbar\kappa}{M}[\psi_1^*(-\mathrm{i}\partial_x - \partial_y)\psi_0 + \psi_0^*(-\mathrm{i}\partial_x - \partial_y)\psi_{-1} + \psi_0^*(-\mathrm{i}\partial_x + \partial_y)\psi_1 + \psi_{-1}^*(-\mathrm{i}\partial_x + \partial_y)\psi_0] + \frac{g_n'}{2}(|\psi_1|^2 + |\psi_0|^2 + |\psi_{-1}|^2)^2 + \frac{g_s'}{2}[(|\psi_1|^2 - |\psi_{-1}|^2)^2 + 2|\psi_1^*\psi_0 + \psi_0^*\psi_{-1}|^2]\Big\} \quad (15)$$

where $g_n' = \sqrt{\frac{M\omega_z}{2\pi\hbar}}g_n$, $g_s' = \sqrt{\frac{M\omega_z}{2\pi\hbar}}g_s$.

The spin–orbit coupled spinor condensate can develop a plane wave phase [see Fig. 4(a)] or stripe phase [see Fig. 4(b)] due to the interaction energy [66–68]. In this

condition, the characteristic length of the harmonic external potential is much greater than the wavelength of the stripe, meaning a weak external trap compared to the spin–orbit coupling strength. Trapped spin-1 BECs with neither too strong nor too weak spin–orbit coupling strength, however, are less studied. In this case, the atom–atom interaction should be large enough to produce trapped plane wave or stripe state. In the trapped plane wave or stripe state, we find there exist nontrivial detailed structures, as we will see in the following paragraphs.

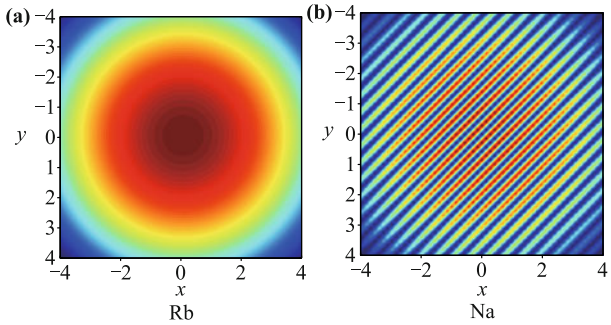

Fig. 4 The density profile of the component with magnetic quantum number $k = 1$ spin component in the plane wave phase **(a)** and stripe phase **(b)**.

The spin is accompanied by a magnetic moment, resulting in magnetism. The Zeeman field can be used to explore quantum characters of the spinor BECs, for instance, applied external Zeeman field can induce the coherent dynamics in the spin-1 BECs [69]. Zeeman field can produce a rich ground state phase diagram via tuning their magnetization [4, 70]. As pointed out in Ref. [4], a broken-axisymmetry state rises as an intermediate phase between the ferromagnetic and polar phases, showing the magnetic system responds to the external magnetic field in a very unique manner. Thus, an external Zeeman field on the spin–orbit coupled BECs.

For the quasi-two-dimensional Rashba type spin–orbit coupled spin-1 BEC within the Zeeman field, the energy functional in the mean-field approximation can be written as [71]

$$\begin{aligned} H = \int \mathrm{d}r \Big\{ & \sum_m \psi_m^* \Big(-\frac{\hbar^2 \nabla^2}{2M} - pm + qm^2 \Big) \psi_m \\ & + \frac{\hbar\kappa}{M} [\psi_1^* (-\mathrm{i}\partial_x - \partial_y)\psi_0 + \psi_0^* (-\mathrm{i}\partial_x - \partial_y)\psi_{-1} + h.c.] \\ & + \frac{g_n'}{2} n^2 + \frac{g_s'}{2} [(n_1 - n_{-1})^2 + 2|\psi_1^* \psi_0 + \psi_0^* \psi_{-1}|^2] \Big\} \end{aligned} \tag{16}$$

where $m = 1, 0, -1$ and the density distribution of the component m reads $n_m = |\psi_m|^2$ with the condensation wave function ψ_m, thus the total atomic density is $n = \sum_m n_m$.

In the presence of the linear Zeeman field only, the single-particle energy spectrum is

$$\begin{aligned} E_0 &= E_{\boldsymbol{k}} \\ E_\pm &= E_{\boldsymbol{k}} \pm \sqrt{p^2 + \frac{4\kappa^2}{M} E_{\boldsymbol{k}}} \end{aligned} \tag{17}$$

And in the presence of the quadratic Zeeman field only, we have

$$\begin{aligned} E_0 &= E_{\boldsymbol{k}} + q \\ E_\pm &= E_{\boldsymbol{k}} + \frac{1}{2} q \pm \frac{1}{2} \sqrt{q^2 + \frac{16\kappa^2}{M} E_{\boldsymbol{k}}} \end{aligned} \tag{18}$$

where $E_{\boldsymbol{k}} = \hbar^2 k_\perp^2 / (2M)$, and the subscript $\pm$ denotes the helicity branches of spin parallel or antiparallel to wave vector. The single-particle ground states are of the negative helicity with the momentums $k_\perp = \sqrt{\frac{2\kappa^2}{\hbar^2} - \frac{M^2 p^2}{2\hbar^2 \kappa^2}}$ in linear Zeeman field and $k_\perp = \sqrt{32\kappa^4 - 2q^2 M^2}/(4\hbar\kappa)$ in quadratic Zeeman field, respectively. Corresponding to the negatice helicity branch, the single-particle eigenstates are given by

$$\Psi_{\boldsymbol{k}} = \begin{pmatrix} \alpha_1 \\ -\alpha_0 \mathrm{e}^{\mathrm{i}\theta} \\ \alpha_{-1} \mathrm{e}^{\mathrm{i}2\theta} \end{pmatrix} \mathrm{e}^{\mathrm{i}\boldsymbol{k}\cdot\boldsymbol{r}} \tag{19}$$

where $\theta = \arctan(k_y/k_x)$, and α_m $(\sum_m \alpha_m^2 = 1)$ are

$$\begin{aligned} L: \quad & \alpha_1 = \frac{2\kappa^2 + Mp}{4\kappa^2}, \quad \alpha_{-1} = \frac{2\kappa^2 - Mp}{4\kappa^2} \\ & \alpha_0 = \sqrt{2\alpha_1 \alpha_{-1}} \\ Q: \quad & \alpha_1 = \alpha_{-1} = \frac{\sqrt{4\kappa^2 - Mq}}{4\kappa} \\ & \alpha_0 = \frac{\sqrt{2}\sqrt{4\kappa^2 + Mq}}{4\kappa} \end{aligned} \tag{20}$$

where L and Q represent the energy spectrums in linear and quadratic Zeeman fields, respectively. From the single-particle energy spectrum above, we can see the Zeeman effects shift the momentum of ground state compared to the case in absence of external magnetic field.

In two dimensional homogeneous system, the ground states of the spin–orbit coupled condensate are circularly degenerate. The atomic interactions (the interaction preserves the symmetries of single particle Hamiltonian) intend to couple different single particle states and the ground state which preserves the $\mathcal{C}_{nz}$ symmetry can be approximately described by the linear superposition of single-particle eigenstates on the degenerate momentum ring, $\Psi = \sum_n \mathcal{A}_n \Psi_{\boldsymbol{k}}$ with $\mathcal{A}_n$ satisfying $\sum_n |\mathcal{A}_n|^2 = 1$ (n is an non-negative integer [67]). By substituting the ansatz into Eq. (16), it is shown that these high-symmetry states with $n \geqslant 3$ are energetically

unfavored. Thus, we can assume

$$\Psi = \mathcal{A}\Psi_{\boldsymbol{k}} + \mathcal{B}\Psi_{-\boldsymbol{k}} \tag{21}$$

where, the coefficients $\mathcal{A}$ and $\mathcal{B}$ are real constants satisfying the normalization condition $\mathcal{A}^2 + \mathcal{B}^2 = 1$. The approximate ground state can be obtained by minimizing the energy function in Eq. (16) after the substitution of Eq. (21).

In the presence of the Zeeman field, the boundary between plane wave and stripe phases are determined by $\xi = (2 - M^2p^2/\kappa^4)g_s' + \frac{M^4p^4}{16\kappa^8}(g_s' - g_n')$ (in the presence of the linear Zeeman field only) or $\xi = 2g_s' - \frac{M^2q^2}{16\kappa^4}(2g_s' + g_n')$ (in the presence of the quadratic Zeeman field only), where $\xi = [2\alpha_0^2(\alpha_1^2 + 6\alpha_1\alpha_{-1} + \alpha_{-1}^2) - (\alpha_1^2 - \alpha_{-1}^2)^2]g_s' - (\alpha_1^2 - \alpha_0^2 + \alpha_{-1}^2)^2 g_n'$. In Fig. 5 (the numerical results obtained by imaginary time evolution are also shown), we show the phase diagram with respect to the parameters (g_s', p) and (g_s', q). We can observe that the stripe phase only exists in the case of $g_s' > 0$. In addition, the phase transition from the stripe to plane wave phase would occur when the strength of magnetic field surpasses the critical value $p_0 = 2\kappa^2\sqrt{(\sqrt{2g_s'^2 + 2g_s'g_n'} - 2g_s')/[M^2(g_n' - g_s')]}$ for the linear Zeeman field case, and $q_0 = 4\kappa^2\sqrt{2g_s'/[(g_n' + 2g_s')M^2]}$ for the quadratic case.

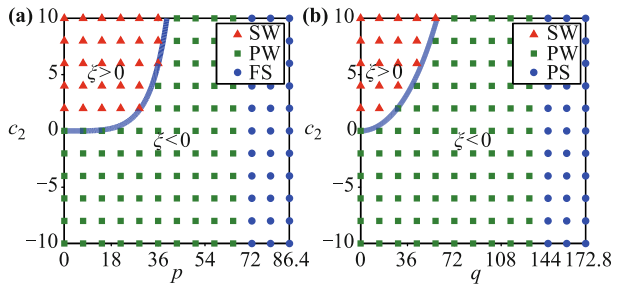

Fig. 5 **(a)** The phase diagram of mean-field ground state in linear Zeeman field. **(b)** The phase diagram of mean-field in quadratic Zeeman field. The red triangles and green squares respectively denote the stripe (SW) and plane wave (PW) phases given by numerical results, and the blue line is the phase boundary $\xi = 0$ between these two phases. The blue circles represent the zero momentum ferromagnetic state (FS) in (a) and the zero momentum polar state (PS) in (b), respectively. The other parameters in both the figures are $g_n' = 100$, $M = 1$ and $\kappa = 6$. Reproduced from Ref. [71], Copyright © 2012 American Physical Society.

In particular, the system can be polarized by the magnetic field if the strength of linear (or quadratic) Zeeman effect attain the critical values $p_m = 2\kappa^2/M$ (or $q_m = 4\kappa^2/M$), and all the atoms occupy the state ψ_1 (or ψ_0) with zero momentum.

3.3 Testing the ground state

In Ref. [72], the superfluidity–Mott-insulator transition of cold atoms in optical lattices was probed by using cavity transmission spectra. As shown above in the spin-1 condensate in the absence of the spin–orbit coupling, there are two possibilities for the ground state, i.e. the ferromagnetic state and the polar state. These two phases are different in the aspect of rotational properties. The polar state is a $SU(2)$ singlet and thus isotropic. However, the ferromagnetic state is a $SU(2)$ multiplet heavily degenerate, and thus can be well directed. From the point view of the quantum phase transition, it is relevant to identify these two phases experimentally [73]. In this section, we focus on the method to distinguish the ferromagnetic and polar quantum ground states by using cavity quantum electrodynamics techniques.

The spin-1 BECs of certain type with total atom number N can be loaded inside an optical cavity [74, 75], and then probed with laser beam which is σ_+ polarized. We choose the bare frequency of the cavity mode ω_c to resolve the alkali D line (fine structure) and lie near the D_1 transition. In addition, we need that the detuning between the D_1 transition and the cavity mode frequency is relatively large, so that the hyperfine structures of the D_1 line would not be resolved. The effective Hamiltonian to describe the atom-cavity photon interaction can be expressed as (see the appendix in Ref. [76])

$$\hat{H}_{int} = \sum_m \left(1 + \frac{m}{2}\right) U_0 \int \mathrm{d}x u^2(x)\hat{\psi}_m^\dagger(x)\hat{\psi}_m(x)a^\dagger a \tag{22}$$

where $\hat{\psi}_m(x)$ $(m = 0, \pm 1)$ is the field annihilation operator for an atom in the hyperfine state $|F = 1, m\rangle$ at position x (the quantization direction is along the cavity axis and is denoted as z-direction), and a is the annihilation operator of the cavity photon; $u(x)$ is the cavity mode function whose maximum is normalized to unity; U_0 describes the strength of the ac-Stark shifts of the atomic levels per photon in the viewpoint of the atoms or alternatively, the magnitude of the cavity frequency shift per atom in the viewpoint of the photons. Based upon the single mode approximation (SMA), the atomic field operators $\hat{\psi}_m(x) = \phi(x)c_m$ [$\phi(x)$ denotes the common spatial mode] and c_m is the annihilation operator corresponding to the spin component with magnetic quantum number m. We can rewrite the Hamiltonian (22) as

$$H_{int} = U_d\left(\hat{N} + \frac{1}{2}\hat{M}\right)a^\dagger a \tag{23}$$

where $\hat{N} = \sum_m c_m^\dagger c_m$ is the total atom number and $\hat{M} = \sum_m m c_m^\dagger c_m$ the total magnetization; $U_d \equiv U_0 \int \mathrm{d}x u^2(x)\phi^2(x)$, which can be approximated by $U_d \simeq U_0/2$ [76].

We assume that the frequency of the probe laser is ω_p,

and the Heisenberg equation of the cavity mode annihilation operator in the frame rotating at ω_p is

$$\dot{a} = -\mathrm{i}\left[\omega_c - \omega_p + U_d\left(\hat{N} + \frac{1}{2}\hat{M}\right)\right]a - \kappa_0 a + \eta \quad (24)$$

where κ_0 and η are the damping rate of the cavity mode and the driving amplitude respectively. There exists stationary solution of the photon number operator and the corresponding expectation value is

$$n_{st} = \langle \hat{n}_{st} \rangle = \sum_{M=-N}^{N} f_M \frac{\eta^2}{\kappa_0^2 + (\Delta + U_d M/2)^2} \quad (25)$$

where $\Delta = \omega_c + U_d N - \omega_p$ is the shifted cavity-probe detuning and f_M the probability for $\hat{M}$ taking value M in the prescribed state satisfying $\sum_M f_M = 1$. From Eq. (25), we can find that the cavity transmission spectra which is proportional to n_{st} contains information of the atomic statistics embodied in f_M.

Now Eq. (25) can be used to identify the two phases of the spin-1 BECs: polar and ferromagnetic phases. For the polar phase, the total spin is $f = 0$ and we have the intracavity photon number like

$$n_{st}(\Delta) = \frac{\eta^2}{\kappa_0^2 + \Delta^2} \quad (26)$$

We should notice that it is of the same shape as that of a bare cavity. For the ferromagnetic phase, we start our discussion by considering the most experimentally accessible states [77] – angular momentum coherent states, which can be obtained by rotating the z-aligned state $|N, N\rangle$. The coherent state can be expressed as

$$\mathrm{e}^{-\mathrm{i}\theta\boldsymbol{\zeta}\cdot\boldsymbol{F}}|N, N\rangle = \frac{(x_{+1}c_{+1}^{\dagger} + x_0 c_0^{\dagger} + x_{-1}c_{-1}^{\dagger})^N}{\sqrt{N!}}|0\rangle \quad (27)$$

where $\boldsymbol{\zeta} = (-\sin\phi, \cos\phi, 0)$ is the axis of rotation and θ is the angle of rotation. x_i's are determined by $\mathrm{e}^{-\mathrm{i}\theta\boldsymbol{\zeta}\cdot\boldsymbol{F}}c_{+1}^{\dagger}\mathrm{e}^{\mathrm{i}\theta\boldsymbol{\zeta}\cdot\boldsymbol{F}} = x_{+1}c_{+1}^{\dagger} + x_0 c_0^{\dagger} + x_{-1}c_{-1}^{\dagger}$. The intracavity photon number n_{st} can be obtained as

$$n_{st}(\Delta) = \frac{\eta^2}{2\kappa_0}\int_{-\infty}^{+\infty} \mathrm{d}t \mathrm{e}^{\mathrm{i}t(\Delta-\Delta_c)} \times \mathrm{e}^{-\kappa_0|t| - t^2 U_d^2 \sigma^2/8} \quad (28)$$

where $\Delta_c = -M_c U_d/2$ ($M_c = N\cos\theta$) and $\sigma = \sqrt{N}\sigma_0$ ($\sigma_0 = \sqrt{\frac{1}{2}\sin^2\theta}$).

From Eq. (28), we obtain the following conclusions: (1) Due to the average deviation of M from zero, the shape of n_{st} as a function of Δ is shifted by Δ_c comparing with that in Eq. (26). (2) Due to the fluctuations of M around the mean, the shape of n_{st} is broadened.

In Fig. 6, the intracavity photon number as a function of the detuning Δ is plotted. For the polar state, the curve (solid line) is simple Lorentzian distribution centered at $\Delta_c = 0$ and with width $2\kappa_0$. For the ferromagnetic ground states, however, the center and width of the curve vary widely depending on the inclination angle θ (we have artificially shifted the curves to a common center; see the labels of the horizontal axes). Consequently, the polar and ferromagnetic ground states can be well distinguished by referring to the different shapes of the corresponding spectra.

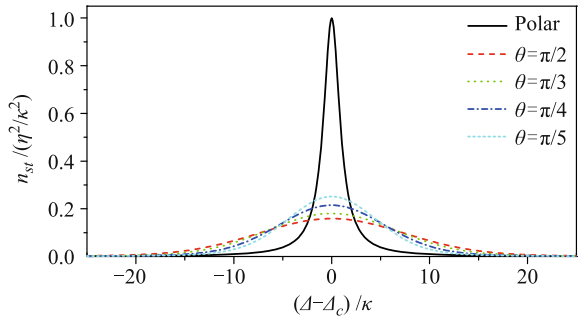

Fig. 6 Intracavity photon number at steady state as a function of the detuning Δ. The solid line corresponds to the polar ground state. Other lines correspond to ferromagnetic ground states. The parameters are $N = 10^6$ and $U_d = 0.01\kappa_0$. For the horizontal labels, $M_c = N\cos\theta$ and $\Delta_c = -M_c U_d/2$ in the ferromagnetic case, while $M_c = 0$ and $\Delta_c = 0$ in the polar case. Reproduced from Ref. [76], Copyright © 2009 American Physical Society.

4 Solitons

The competition between the nonlinearity and dispersion leads to the appearance of the localized wave structures, such as bright solitons (arise in the BECs with attractive interaction between atoms), dark soliton (arise in the BECs with repulsive interaction between atoms) and vortices. In this section, we will focus on this topic and have a review of our recent theoretical advances in this nonlinear matter wave state, including magnetic solitons [76], one-, two-, three-component solitons of the polar and ferromagnetic types, and ring dark solitons.

4.1 One dimensional solitons

Explorations on the spinor BECs trapped in optical lattices show that if the optical lattices are deep enough for the individual sites to be independent, the system can undergo a ferromagnetic like phase transition that leads to a "macroscopic" magnetization [79, 80]. Thus, the spinor BEC at each lattice site would behave like a spin magnet. As a consequence, the light-induced dipole–dipole interaction and the static magnetic dipole–dipole interaction cannot be ignored. These dipolar interactions can induce the ferromagnetic phase transition and spin-wave excitations [81]. In this section, we will show that the magnetic solitons would arise in the spinor BECs confined in a one-dimensional optical lattice because of the interactions between the spin waves. The character-

istics of these magnetic soliton can be tuned by the light-induced and the magnetic dipole–dipole interactions.

There are three types of two-body interactions for spinor BECs trapped in optical lattices: spin-change collision, magnetic dipole–dipole interaction and light-induced dipole–dipole interaction. The Hamiltonian can be written as

$$H=\sum_n\int \mathrm{d}\boldsymbol{r}\hat{\psi}_n^{\dagger}(\boldsymbol{r})[-\frac{\hbar^2\nabla^2}{2m}+V_L(\boldsymbol{r})]\hat{\psi}_n(\boldsymbol{r}) +\sum_{n,m,n',m'}\int \mathrm{d}\boldsymbol{r}\mathrm{d}\boldsymbol{r}'\hat{\psi}_n^{\dagger}(\boldsymbol{r})\hat{\psi}_m^{\dagger}(\boldsymbol{r}')[V_{nn'mm'}^{coll}(\boldsymbol{r},\boldsymbol{r}') +V_{nn'mm'}^{d-d}(\boldsymbol{r},\boldsymbol{r}')]\hat{\psi}_{m'}(\boldsymbol{r}')\hat{\psi}_{n'}(\boldsymbol{r})+H_B \quad (29)$$

where $V_L(\boldsymbol{r})$ is the lattice potential, and the index $n,m,n',m'=-1,0,1$ denotes the Zeeman sublevels of the ground state of the atoms. $V_{nn'mm'}^{coll}(\boldsymbol{r},\boldsymbol{r}')$ describes the two-body ground-state collisions, $V_{nn'mm'}^{d-d}(\boldsymbol{r},\boldsymbol{r}')$ include magnetic dipole–dipole interaction and light induced dipole–dipole interaction, and H_B represents the external magnetic interaction.

When the depth of the optical lattice is deep enough, the spinor atomic field operator can be expressed as $\hat{\psi}_m(\boldsymbol{r})=\sum_i\phi_i(\boldsymbol{r})C_m(i)$, where $\phi_i(\boldsymbol{r})$ is the condensate wave function for the *ith* microtrap and the operators $\hat{C}_m(i)$ satisfy the bosonic commutation relations $[\hat{C}_m(i),\hat{C}_n^{\dagger}(j)]=\delta_{mn}\delta_{ij}$. By using the tight-binding approximation and the Holstein–Primakoff transformation method [82], we can obtain the Hamiltonian in the first-order approximation:

$$H=-\gamma_B NSB_z-J^zZNS^2+\sum_i\gamma_B B_z a_i^{+}a_i +2ZJ^zS\sum_i a_i^{+}a_i-2SJ\sum_{i\delta}(a_i^{+}a_{i+\delta}+a_ia_{i+\delta}^{+}) \quad (30)$$

where $\gamma_B=-\mu_B g_F$, with μ_B being the Bohr magneton and g_F the Landé g factor; $N=\sum_i N_i$ is the total atomic number in the lattice; S and Z are the local maximum spin and coordination number of the lattice; B_z is the magnitude of the magnetic field which is along z direction; the creation and annihilation boson operators a,a^{+} are introduced to represent the spin operators. We have assumed that $J=J_{ij}=J_{ij}^{ld}-\frac{1}{4}J_{ij}^{md}$, J_{ij}^{md} is a coefficient which represent magnetic dipole-dipole interaction and J_{ij}^{ld} is a coefficient which represents light induced dipole–dipole interaction.

Then we can obtain the dispersion relation of the spin wave:

$$\hbar\omega_k=-\gamma_B B_z+\sum_{\delta>0}[4J^{md}S-8SJ\cos(\delta k)] \quad (31)$$

We can find that the dispersion relation of the spin wave can be easily tuned by the dipole–dipole interaction in the optical lattice.

We can get further on our way to include higher order terms. Thus the hamiltonian can be expressed as (omitting the fourth order term):

$$H=\lambda_a^{'}NS(S+1)-\gamma_B B_zSN+\gamma_B B_z\sum_i a_i^{+}a_i -\sum_i\sum_{j\neq i}(J_{ij}^{md}S^2-J_{ij}^{md}Sa_j^{+}a_j-J_{ij}^{md}Sa_i^{+}a_i +J_{ij}^{md}a_i^{+}a_ia_j^{+}a_j)-\sum_i\sum_{j\neq i}(2J_{ij}Sa_i^{+}a_j +2J_{ij}Sa_ia_j^{+})+\frac{1}{2}\sum_i\sum_{j\neq i}J_{ij}(a_i^{+}a_i^{+}a_ia_j +a_i^{+}a_j^{+}a_ja_j+a_ja_i^{+}a_i^{+}a_i+a_j^{+}a_ja_ja_i^{+})+\cdots \quad (32)$$

In the following part, we will find that the hight order terms will bring into appearance the soliton type nonlinear excitations.

In the ideal case, we can assume that the spinor condensate in the optical lattice should initially be prepared in a spin-coherent state $|\psi\rangle=|\{\psi_l\}\rangle=\Pi_l\ |\psi_l\rangle$, with $|\psi_l\rangle=\exp(-|\psi_l|^2/2)\exp(-\psi_l a^{+})|0\rangle$. The vacuum state $|0\rangle$ is the ground state of the BEC in the optical lattice, i.e., $|0\rangle=|GS\rangle=|N,-N\rangle$ [82]. The dynamics of the probability amplitude describing the nonlinear dynamics of coherent spin excitations on the lattice l can be derived as

$$\mathrm{i}\hbar\frac{\partial\psi_l}{\partial t}=(\gamma_B B_z+4J_{MD}S-8JS)\psi_l+4JS(2\psi_l -\psi_{l+1}-\psi_{l-1})-2J_{MD}(|\psi_{l-1}|^2+|\psi_{l+1}|^2)\psi_l +J(|\psi_{l+1}|^2\psi_{l+1}+|\psi_{l-1}|^2\psi_{l-1}+2|\psi_l|^2\psi_{l+1} +2|\psi_l|^2\psi_{l-1})+J(\psi_{l+1}^{+}+\psi_{l-1}^{+})\psi_l^2 \quad (33)$$

The nearest-neighbor interactions are considered only, which is reasonable for the BECs in one dimension optical lattice [83]).

In the long-wavelength limit and by considering the continuum limit approximation we consider $\psi_l,\psi_{l+1},\psi_{l-1}\to\psi(z,t)$. We then obtain the following soliton solutions which are characterized by parameters $\xi_1=4JS=4S(J_{LD}-J_{MD}/4)$ and $\xi_2=(4J_{MD}-8J)=6J_{MD}-8J_{LD}$, where J_{MD} and J_{LD} are the average values of J_{ij}^{md} and J_{ij}^{ld}, respectively.

(i) When $J_{LD}<J_{MD}/4$, $\xi_1<0$, and $\xi_2>0$, there is single dark soliton solution:

$$\psi(z,t)=\sqrt{-\frac{\xi_2}{\xi_1}}\tanh\left[-\frac{\xi_2}{\sqrt{2}\xi_1}(z-vt)\right] \cdot\exp[\mathrm{i}(\gamma_0 z-\omega_1 t)] \quad (34)$$

where $\hbar\omega_1=\gamma_B B_z+4J^zS-8JS-\xi_1v^2/4-2\xi_2^2/|\xi_1|$ is

the single dark soliton energy, and $\gamma_0 = v/2$, where v is the velocity of the soliton.

(ii) When $\frac{3}{4}J_{MD} > J_{LD} > \frac{1}{4}J_{MD}$, $\xi_1 > 0$, and $\xi_2 > 0$, there is bright magnetic soltion solution like

$$\psi(z,t) = \sqrt{\frac{\xi_2}{\xi_1}} sech\left[\frac{\xi_2}{\xi_1}(z - vt)\right] \exp[\mathrm{i}(\gamma_0 z - \omega_2 t)] \quad (35)$$

where $\hbar\omega_2 = \gamma_B B_z + 4J^z S - 8JS + \xi_1 v^2/4 - 2\xi_2^2/\xi_1, \gamma_0 = v/2, v$ is the velocity of the soliton.

For both solutions, the energy of the soliton is smaller than the spin wave. Most importantly, the width and amplitude of the above nonlinear matter waves can be directly manipulated by tuning the light induced or magnetic dipole–dipole interactions.

Next, we are going to review the soliton solutions in Ref. [35] obtained by solving the one dimension nonlinearly coupled Gross–Pitaevskii equations, which can be derived from the three dimension nonlinearly coupled Gross–Pitaevskii equations. The one dimension nonlinearly coupled Gross–Pitaevskii equations are [22, 84]

$$\begin{aligned}
\mathrm{i}\hbar\partial_t\psi_{\pm1} &= -\frac{\hbar^2}{2M}\partial_x^2\psi_{\pm1} + (c_0 + c_2)(|\psi_{\pm1}|^2 + |\psi_0|^2)\psi_{\pm1} \\
&\quad + (c_0 - c_2)|\psi_{\mp1}|^2\psi_{\pm1} + c_2\psi_{\mp1}^*\psi_0^2 \\
\mathrm{i}\hbar\partial_t\psi_0 &= -\frac{\hbar^2}{2M}\partial_x^2\psi_0 + (c_0 + c_2)(|\psi_1|^2 + |\psi_{-1}|^2)\psi_0 \\
&\quad + c_0|\psi_0|^2\psi_0 + 2c_2\psi_0^*\psi_1\psi_{-1} \qquad (36)
\end{aligned}$$

where $c_0 = \left\{4\hbar^2 a_0/[Ma_\perp^2(1 - ca_0/a_\perp)] + 24\hbar^2 a_2/[Ma_\perp^2(1 - ca_2/a_\perp)]\right\}/3$ and $c_2 = \left\{4\hbar^2 a_2/[Ma_\perp^2(1 - ca_2/a_\perp)] - 4\hbar^2 a_0/[Ma_\perp^2(1 - ca_0/a_\perp)]\right\}/3$ denote the mean-field interaction and the spin-exchange interaction, respectively [85]. $a_\perp$ is the characteristic length of the condensate in the transverse direction and $c = -\zeta(1/2) = 1.46$. Introducing the transformation $(\psi_1, \psi_0, \psi_{-1})^{\mathrm{T}} \to (\phi_1, \sqrt{2}\phi_0, \phi_{-1})^{\mathrm{T}}$ and the time and length are measured in units of $\hbar/|c_0|$ and $\sqrt{\hbar^2/(2M)|c_0|}$, respectively, then Eqs. (36) become

$$\begin{aligned}
\mathrm{i}\partial_t\phi_{\pm1} &= -\partial_x^2\phi_{\pm1} - (\nu + a)(|\phi_{\pm1}|^2 + 2|\phi_0|^2)\phi_{\pm1} \\
&\quad - (\nu - a)|\phi_{\mp1}|^2\phi_{\pm1} - 2a\phi_{\mp1}^*\phi_0^2 \\
\mathrm{i}\partial_t\phi_0 &= -\partial_x^2\phi_0 - (\nu + a)(|\phi_1|^2 + |\phi_{-1}|^2)\phi_0 \\
&\quad - 2\nu|\phi_0|^2\phi_0 - 2a\phi_0^*\phi_1\phi_{-1} \qquad (37)
\end{aligned}$$

where $\nu = -c_0/|c_0|$ and $a = -c_2/|c_0|$.

For the particular integrable case $\nu = a = 1$, solitons in the model of spinor BEC have been studied in Ref. [22]. For $\nu \neq a$, there are exact soliton solutions of polar or ferromagnetic type.

(i) Single-component ferromagnetic soliton ($a + \nu > 0$)

$$\phi_{-1} = \phi_0 = 0,\ \phi_{+1} = \sqrt{\frac{-2\mu}{\nu + a}}\mathrm{e}^{-\mathrm{i}\mu t}\mathrm{sech}(\sqrt{-\mu}x) \quad (38)$$

Negative chemical potential μ is the intrinsic parameter of this soliton family. From solution (38), moving soliton solutions can be obtained by means of Galilean transformation. By using linearized equations for small perturbations, this solution is demonstrated to be stable against infinitesimal perturbations.

(ii) Single-component polar soliton ($\nu = +1$)

$$\phi_{\pm1} = 0,\ \phi_0 = \sqrt{-\mu}\mathrm{e}^{-\mathrm{i}\mu t}\mathrm{sech}(\sqrt{-\mu}x) \quad (39)$$

By means of direct simulations with a small random perturbation being distributed uniformly between 0 and 0.03, we find that this soliton solution is always unstable in the region of $a < -1/4$.

(iii) Two-component polar soliton ($\nu = +1$)

$$\phi_0 = 0,\ \phi_{\pm1} = \sqrt{-\mu}\mathrm{e}^{-\mathrm{i}\mu t}\mathrm{sech}(\sqrt{-\mu}x) \quad (40)$$

Direct simulations show that the soliton is indeed unstable in the region of $|a| \geqslant 1$, and stable if $|a| < 1$.

(iv) Three-component polar solitons

$$\begin{aligned}
\phi_0 &= (\mu_{+1}\mu_{-1})^{1/4}\mathrm{sech}(\sqrt{-\mu}x)\mathrm{e}^{-\mathrm{i}\mu t} \\
\phi_{\pm1} &= \sqrt{-\mu_{\pm1}}\mathrm{e}^{-\mathrm{i}\mu t}\mathrm{sech}(\sqrt{-\mu}x) \qquad (41)
\end{aligned}$$

This three-component polar soliton is completely stable and this point has been checked in detail by seeding small random perturbations in all the components.

By comparing respective values of the Hamiltonian for these solutions when the atom number is fixed, we find that the single-component ferromagnetic soliton and the stable three-component polar soliton simultaneously provide for the minimum of energy in the case of $\nu = +1$ and $a > 0$. For $\nu = +1$ and $-1 < a < 0$ (attractive spin-independent and repulsive spin-exchange interactions), the two-component polar soliton plays the role of the ground state. Finally, for $\nu = +1$ and $a < -1$, there are no stable solitons (among the ones considered above).

4.2 Two dimensional solitons

Solitons in quasi-one dimension can live long lifetimes [86, 87]. But it is not the case in high dimensional cases. In two dimensional case, most types of solitons only live a short lifetime due to the dynamical instability arising from the higher dimensionality. As pointed out in Ref. [88], dark lumplike and dark stripe solitons will decay into vortex pairs under small transverse perturbations. However, there is candidate for observing long-lived dark soliton: ring dark soliton. The concept of ring dark soliton was first introduced and experimentally realized in nonlinear optics [89–91]. In this section, we will go through the dynamical generation and evolution of the ring dark solitons in $F = 1$ ^{23}Na and ^{87}Rb condensates by modeling the phase engineering technique in the

experiments [92].

Matter-wave dark solitons can be created experimentally by using the phase engineering and density engineering techniques [93–97]. As a great progress in this technique, Wright *et al*. [98] have realized spatially varying control of both the amplitude and the phase of the spinor order parameter.

In the experiment, a far-off resonant laser pulse is passed through an absorption plate (to modulate the spatial distribution of the intensity of the laser beam), and then space-dependent conservative Stark-shift potential can be created, leading to a space-dependent phase shift in the condensate order parameter. In Fig. 7 we show the schematic for the generation of ring dark solitons by using the phase engineering technique. The laser beam illuminated onto the condensate generate an effective potential, resulting in phase distributions in the condensate order parameter. The duration of the laser beam pulse is denoted as δt, which must be much smaller than the correlation time of the condensate. The phase step generated on the condensate order parameter can be adjusted by varying δt. The following model can be used to describe the phase distribution after the illustration of the laser beam pulse:

$$\phi(x,y)=\frac{\Delta\phi}{2}\times\left[1+\tanh\left(\frac{R_0-\sqrt{x^2+y^2}}{\Delta x}\right)\right] \quad (42)$$

where $\Delta\phi$ and R_0 characterize the total phase difference and the radius of the ring dark soliton, respectively. Δx reveals the width of the potential edge (induced by the laser beam).

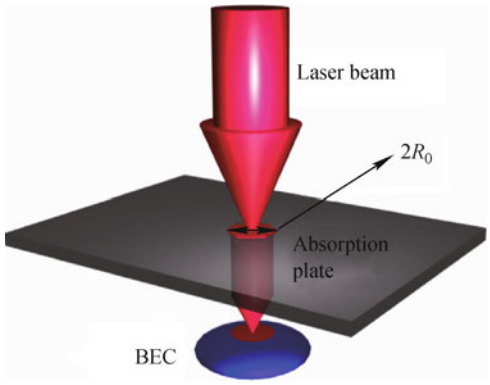

Fig. 7 A schematic of imprinting phase steps onto the condensate. The far-off resonant laser pulse (*light red*) goes through an absorption plate (*gray*), which is used to modulate the laser. The modulated laser pulse illuminates the cold-atomic condensate (*blue*) and produces an expected phase configuration. Here, R_0 is the radius of the ring dark soliton that is to be created. Reproduced from Ref. [92], Copyright © 2012 American Physical Society.

We choose that $\omega_\perp=\omega_x=\omega_y=(2\pi)\times 12$ Hz and $\omega_z=(2\pi)\times 372$ Hz, respectively, which is feasible experimentally. And the quasi-two dimension multicomponent Gross–Pitaevskii equations are

$$\begin{aligned}
\mathrm{i}\hbar\frac{\partial\psi_1}{\partial t}&=\left(-\frac{\hbar^2}{2M}\nabla^2+U\right)\psi_1+(g_n'+g_s')(|\psi_1|^2+|\psi_0|^2)\psi_1\\
&\quad+(g_n'-g_s')|\psi_{-1}|^2\psi_1+g_s'\psi_0^2\psi_{-1}^*\\
\mathrm{i}\hbar\frac{\partial\psi_0}{\partial t}&=\left(-\frac{\hbar^2}{2M}\nabla^2+U\right)\psi_0+(g_n'+g_s')\big(|\psi_1|^2\\
&\quad+|\psi_{-1}|^2\big)\psi_0+g_n'|\psi_0|^2\psi_0+2g_s'\psi_1\psi_0^*\psi_{-1}\\
\mathrm{i}\hbar\frac{\partial\psi_{-1}}{\partial t}&=\left(-\frac{\hbar^2}{2M}\nabla^2+U\right)\psi_{-1}+(g_n'+g_s')\big(|\psi_{-1}|^2\\
&\quad+|\psi_0|^2\big)\psi_{-1}+(g_n'-g_s')|\psi_1|^2\psi_{-1}+g_n'\psi_0^2\psi_1^*
\end{aligned} \quad (43)$$

where $U=\frac{1}{2}M\Omega^2(x^2+y^2)$ and $\Omega=\omega_\perp/\omega_z$. Based on the above two dimensional Gross–Pitaevskii equations (43), we are going to observe the dynamical properties of ring dark solitons in spin-1 BECs (the ground states are obtained by imaginary time evolution method).

The numerical calculations show that the lifetime of the ring dark solitons in spin-1 condensate is largely prolonged. If each component of the condensate puts forth the same parameterized ring dark solitons, then the total density distribution of the condensate exhibits the same profile as that in each component. According to Refs. [99–101] and our numerical calculations, we find that in the ^{87}Rb condensate, the lifetime of the nearly black ring soliton in spinor BEC without Feshbach resonance management is prolonged evidently compared to that in scalar BEC, and this lifetime is comparable with the lifetime of a shallower ring dark soliton (the total phase difference is $\Delta\phi=0.707\pi$) in Ref. [99]. By utilizing the Feshbach technique or varying the parameters of the external potentials and the spin-dependent, -independent interactions, it would be beneficial to prolong the lifetime of the ring dark solitons.

As for the decaying dynamics of the ring dark solitons, differences come out in ^{23}Na and ^{87}Rb condensates. We show this point in Fig. 8. At $t=34.22$ ms, nearly black ring dark solitons have formed in both condensates. However, ring dark solitons in the ^{23}Na, live a shorter lifetime compared to that in the ^{87}Rb condensate. Then the ring dark solitons break into x-like or +-like vortex pairs. The characteristic oscillation properties of the vortex pairs are the same as found by Ref. [100] in scalar BEC. The vortex and antivortex pairs oscillate between the x- and +-like configurations and arrange themselves on a ring that periodically shrinks and expands.

When the ring dark soliton is generated in certain components of the condensate, ring dark solitons in other components will be induced. The mutual filling of the

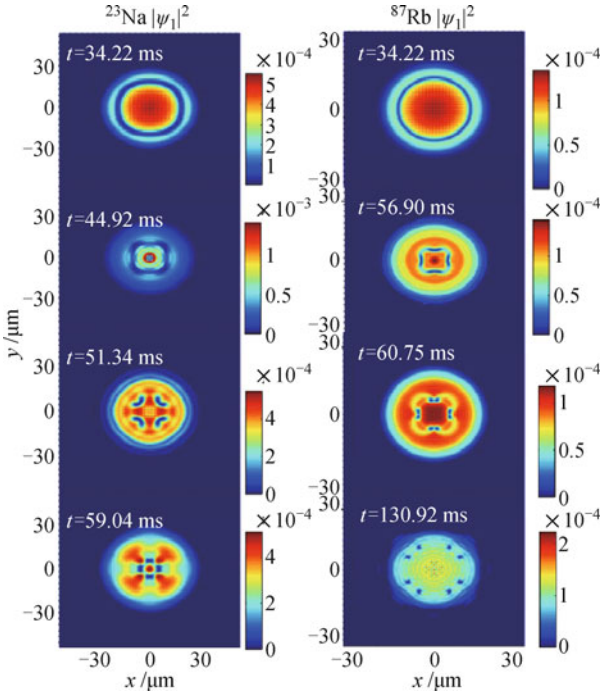

Fig. 8 The density distribution $|\psi_1|^2$ of the decaying ring dark solitons in the ^{23}Na and ^{87}Rb condensates with parameters $N_{Na} = N_{Rb} = 2.5 \times 10^4$, $R_0 = 8.16$ μm, $\Delta\phi = 1.05\pi$ and $\Delta x = 0.56$ μm. Other components of the condensate exhibit the same dynamic configuration. The time and length are measured in units of ω_z^{-1} and $\sqrt{\hbar/(M\omega_z)}$, respectively. Reproduced from Ref. [92], Copyright © 2012 American Physical Society.

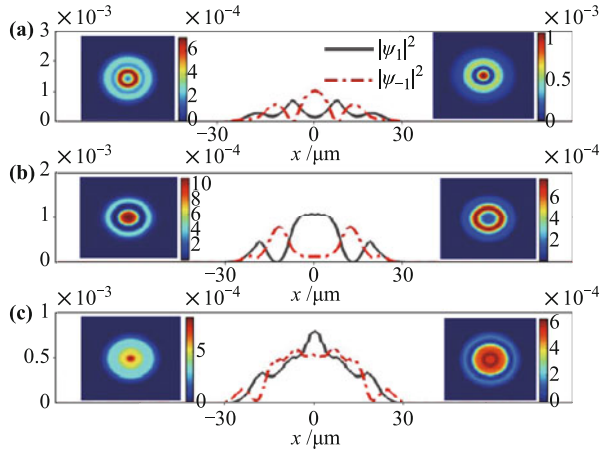

Fig. 9 The 1D density distribution at $t =$ (**a**)67.60, **(b)** 121.50, and **(c)** 159.15 ms in ψ_1 (*solid line*) and ψ_{-1} (*dash-dotted line*) components of the ^{23}Na condensate showing the "darkness-transferring" effect with $N_{Na} = 2.5 \times 10^4$, $R_0 = 8.16$ μm, $\Delta\phi = 1.05\pi$ and $\Delta x = 0.56$ μm. The 2D density distributions according to each time point are attached for ψ_1 (*left*) and ψ_{-1} (*right*). The density of the ψ_0 component (which is of the order of 10^{-8}) is omitted. The time and length are measured in units of ω_z^{-1} and $\sqrt{\hbar/(M\omega_z)}$, respectively. Reproduced from Ref. [92], Copyright © 2012 American Physical Society.

condensates from different components supplies as effective potentials, resulting in a coexistence structure which lives hundreds of milliseconds. Ring dark solitons in both the ^{23}Na and ^{87}Rb condensates show a darkness-transferring phenomenon between different components. Figure 9 shows the dynamical process of the transferring for the ^{23}Na condensate.

The oscillations of the coexistence structure exhibit periodicity roughly and the oscillation frequency is about $0.58\Omega/\sqrt{2}$. We should notice that this oscillation frequency is different from that found in scalar BEC [100, 102]. The periodical property can be found from Fig. 10, which shows the radius of the ring dark soliton varying with respect to the time. Line *a* corresponds to the case of generating the same parameterized ring dark solitons in all three components of the condensate and line *b* the case of generating only one obvious ring dark soliton in one component of the condensate. The oscillation frequency of line *a* is $\omega_o \approx 2.14\Omega/\sqrt{2}$, which is roughly consistent with that in Ref. [100] for the scalar BEC). The oscillation frequency of line *b* is approximately $\omega_o \approx 0.58\Omega/\sqrt{2}$ for line *b*, indicating a prolonged oscillation period. Compared to the 1D condensate, the ring dark soliton oscillates between the maximum and minimum radius with approximately a two-times-larger frequency in the 2D condensate. For the coexistence structure composed of interdependent ring dark solitons from different components of the condensate, the oscillation shows periodic character in a rough way because there are interactions and radiation of the ring dark solitons. In fact, the embedded particles of another component intend to hinder the oscillation of the ring dark solitons, resulting in a low oscillation frequency of the ring dark solitons. Numerical calculations show that ring dark solitons suffers an earlier collapse if an obviously off-centered initial ring dark soliton is used. In addition, ring dark solitons on the coexistence structure of the ferromagnetic condensate incline to decay into vortex and antivortex pairs much earlier than that of the polar condensate.

5 Skyrmion lattices

As a common feature of the fluid systems, vortices have received extensive explorations in diverse fields of science. In fluids without viscosity, quantized vortices come up, which has been well known in liquid helium [103].

For the interactions in BECs can be accurately controlled by means of Feshbach technique [104, 105], explorations of such topological structures in BECs have certain advantages. In Ref. [3], coreless (or Skyrmion) vortices in spin-1 BECs was proposed and such topological structures have attracted much attention [16–19]. In this section we will focus on the topological structures in spin-1 BECs by means of solving the stochastic projected Gross–Pitaevskii equations, which can simulate the dynamics of the condensate at finite temperatures [33, 106,

107].

The nonequilibrium dynamics of a quenched rotating spinor BEC is described by the coupled SPGPEs,

$$\mathrm{d}\psi_j = \mathcal{P}\Big[-\frac{\mathrm{i}}{\hbar}H_j^{GP}\psi_j + \frac{\gamma_j}{k_BT}(\mu - H_j^{GP})\psi_j\Big]\mathrm{d}t + \mathrm{d}W_j \tag{44}$$

where

$$\begin{aligned} H_j^{GP}\psi_j = &\Big[-\frac{\hbar^2\nabla^2}{2M} + V(r) + g_n\sum_{m=0,\pm1}|\psi_m|^2\Big]\psi_j \\ &+g_s\sum_{\zeta=x,y,z}\sum_{n,k,l=0\pm1}(F_\zeta)_{jn}(F_\zeta)_{kl}\psi_n\psi_k^*\psi_l \\ &-\Omega_r L_z\psi_j + \sum_{\zeta=x,y}\sum_{n=0\pm1}\kappa_\zeta(F_\zeta)_{jn}\hat{p}_\zeta\psi_n \end{aligned} \tag{45}$$

Ω_r, $L_z = -\mathrm{i}\hbar(x\partial_y - y\partial_x)$ denote the rotation frequency and the z component of the orbital angular momentum, respectively. $\hat{p}$ and κ_ζ are the momentum operator and the spin–orbit coupling coefficient. In Eq. (44), T, μ and γ_j denote the final temperature, the chemical potential and the growth rate of the j-th component; the complex-valued $\mathrm{d}W_j$ stands for the white noise associated with the condensate growth, which is characterized by the fluctuation-dissipation relation $\langle \mathrm{d}W_i^*(\boldsymbol{x},t)\mathrm{d}W_j(\boldsymbol{x}',t)\rangle = 2\gamma_j\delta_{ij}\delta_C(\boldsymbol{x}-\boldsymbol{x}')\mathrm{d}t$, where δ_C is the Dirac delta function for the condensate band field [27]. The projection operator $\mathcal{P}$ projects the dynamics of the spinor BEC into the energy region below the cutoff energy E_R.

5.1 Spin textures

Topological defects may appear as a consequence of spontaneously broken symmetries. In spinor BECs, it is possible to create topological defects. The interplay between the superfluidity [108] and the magnetism leads to a variety of nontrivial states, for instance, skyrmions, Mermin–Ho vortices, Anderson–Thouless vortices and so on. Topological defects can be created in the phase transitions at finite temperatures according to the Kibble–Zurek scenario and this is because of the spontaneous symmetry breaking and thermal fluctuations around the critical point. By thermally quenching a rotating spin-1 BEC, we find topological defect crystallization of skyrmions appears. For convenience, $U(\boldsymbol{r}) = M\omega^2(x^2 + y^2)/2$ is considered and the oscillator units are chosen in the numerical computations, where the length, time, and energy are respectively scaled in units of $\sqrt{\hbar/(M\omega)}$, $1/\omega$ and $\hbar\omega$.

For the spinor BEC of ^{87}Rb, we show the time evolutions of the density profiles in Fig. 10. We can find that the condensates grow up in the evolution of the evaporative cooling. At the same time, the number of the vortices gets larger and vortices start closely binding up forming into vortex trimers in each component of the condensate. In the interwoven lattice structures, vortex core in one component of the condensate are filled with atoms coming from other components. In other words, quantized vortices avoid overlapping with each other. To characterize these structures, we calculate the incompressible kinetic energy per particle for each component [109] and find the incompressible kinetic energys of different components are different from each other.

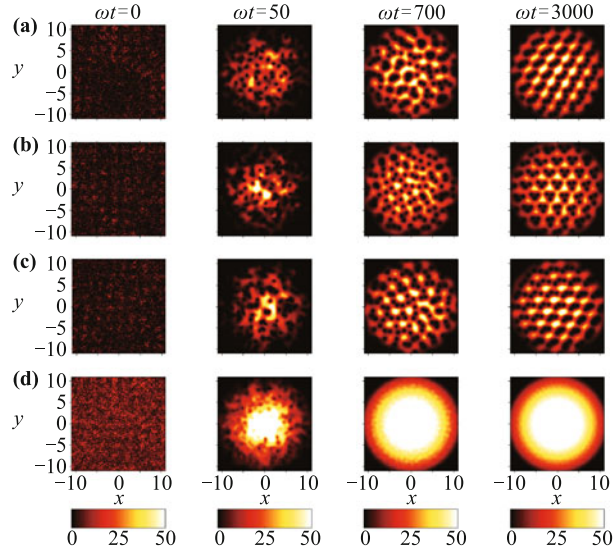

Fig. 10 Snapshots of **(a)** $|\psi_{-1}|^2$, **(b)** $|\psi_0|^2$, **(c)** $|\psi_1|^2$, and **(d)** total density for the quenched rotating spinor BEC of ^{87}Rb. When the system reaches equilibrium at $T = 10$ nK with $\Omega_r = 0.95$, $\mu = 8$ (rightmost column), the crystalline order of vortex trimers is established in each component. The particle numbers in the spinor BEC are $N_{\pm1} \approx 4.84\times10^3$, $N_0 \approx 4.79\times10^3$. Reproduced from Ref. [33], Copyright © 2011 American Physical Society.

In Fig. 11, we plot the spin textures and the topological charge distributions. From Fig. 11(a), we can find that a hexagonal lattice is formed, and Fig. 11(b) shows the spatial variation of the local spin moments parallel to the axis of rotation. Two unit cell of the spin orientations are presented in Fig. 11(c), and This vortex-like arrangement of magnetic moments is in fact the configuration of a skyrmion [110–112]. The topological charge [111] density in Fig. 11(d) shows a hexagonal lattice structure. Numerical integration over the primitive unit cell shows that each skyrmion carries a topological charge $Q = 1$.

For the spinor BEC of ^{23}Na, the vortices lattice is quite different from that of the ^{87}Rb. In the spinor BEC of ^{23}Na, a square lattice of tightly bound vortex dimers emerges in each component. Figure 12 shows the corresponding spin textures and topological charge density distributions. For the spin texture, we find a mosaic of magnetic domains with staggered magnetization is formed, and almost all spins in the domains lie in the

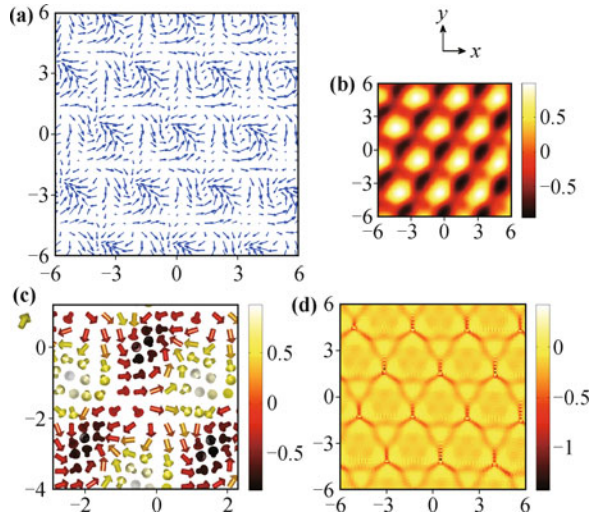

Fig. 11 **(a)** The equilibrium spin textures for the spinor BEC of ^{87}Rb. **(b)** Distribution of $\mathcal{F}_z$ in the spin textures. **(c)** The orientations of the unit spin vector for a skyrmion. The color of each arrow indicates the magnitude of $\mathcal{F}_z$. **(d)** The density profile of the topological charges. Reproduced from Ref. [33], Copyright © 2011 American Physical Society.

x–y plane. It should be noted that the domain walls are narrow and the spins reverse their magnetization through a Bloch wall transition. The staggered magnetic domains usually serve as smoking gun of half quantized vortices [113]. We apply the transformation $(\psi_1, \psi_0, \psi_{-1})^{\mathrm{T}} \rightarrow \hat{G}(\theta)\hat{R}(\boldsymbol{n}, \chi)(\psi_1, \psi_0, \psi_{-1})^{\mathrm{T}}$, where $\hat{G}(\theta)$ and $\hat{R}(\boldsymbol{n}, \chi)$ are the gauge transformation and the spin rotation, respectively. Without loss of generality, we can choose $\boldsymbol{n} = \cos\phi(\boldsymbol{r})\boldsymbol{e}_x + \sin\phi(\boldsymbol{r})\boldsymbol{e}_y$. Numerically, we find that the spin texture will not be changed with $\hat{G}(\pi)\hat{R}(\boldsymbol{n}, \pi)$. Requiring $\hat{G}(\pi)\hat{R}(\boldsymbol{n}, \pi)(\psi_1, \psi_0, \psi_{-1})^{\mathrm{T}} = \mathrm{e}^{\mathrm{i}2\pi}(\psi_1, \psi_0, \psi_{-1})^{\mathrm{T}}$, we can obtain $\mathrm{e}^{-2\mathrm{i}\phi(\boldsymbol{r})}\psi_{-1} = \psi_1$. In Fig. 12(d), we plot the $|\psi_1 - \mathrm{e}^{-2\mathrm{i}\phi(\boldsymbol{r})}\psi_{-1}|$, where the dark shaded region indicates the locations of the polar states while the brightest region means the positions disobeying the transformation, that is, the core of the half quantized vortices.

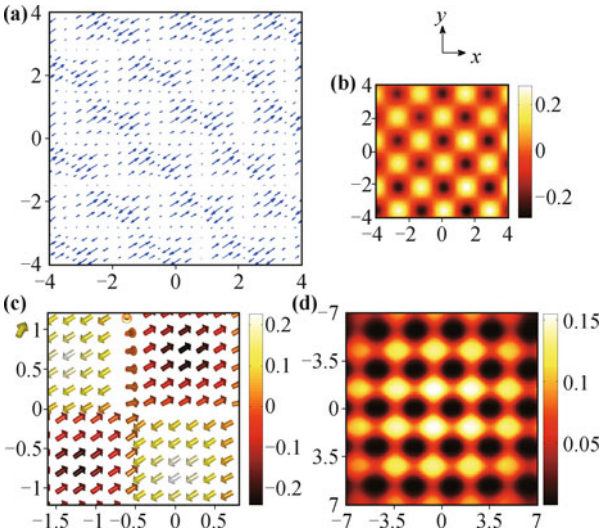

Fig. 12 **(a)** The equilibrium spin textures for the spinor BEC of ^{23}Na. **(b)** Distribution of $\mathcal{F}_z$ in the spin textures. **(c)** The orientations of the unit spin vector in the adjacent magnetic domains. The color of each arrow indicates the magnitude of $\mathcal{F}_z$. **(d)** The modulus of $|\psi_1 - \mathrm{e}^{-2\mathrm{i}\phi(\boldsymbol{r})}\psi_{-1}|$, and the positions of half quantized vortices locate at the brightest regions. Reproduced from Ref. [33], Copyright © 2011 American Physical Society.

So we can conclude that crystallization of skyrmions and half quantized vortices will arise in the spinor BECs.

5.2 Spin–orbit coupled condensate

Spin–orbit coupled spin-1 BECs can lead to half-skyrmion-like excitations (merons), which are peculiar topological defects [114–116]. It is expected that the isolated merons can only be observed when particular boundary conditions are imposed for a meron carrying half a unit of topological charge. Merons can be generated in superfluid ^{3}He-A contained in a rotating cylinder [117, 118] or spinor BECs with a constraining magnetic field [119]. we show in the following paragraphs that stable collective excitations (the crystalline order of merons or other isolated variants) can be created in a rapidly quenched spinor BEC with spin–orbit coupling without rotation ($\kappa_\zeta \neq 0$ and $\Omega_r = 0$).

We begin with the condition of $\kappa_x \neq \kappa_y$. In Fig. 13, density and phase profiles show stripe structures in the process of the condensation. However, the stripe structure in the density profiles inclined to fade away while the system approaches equilibrium. The stripe structure in the phase profiles remains, showing that the

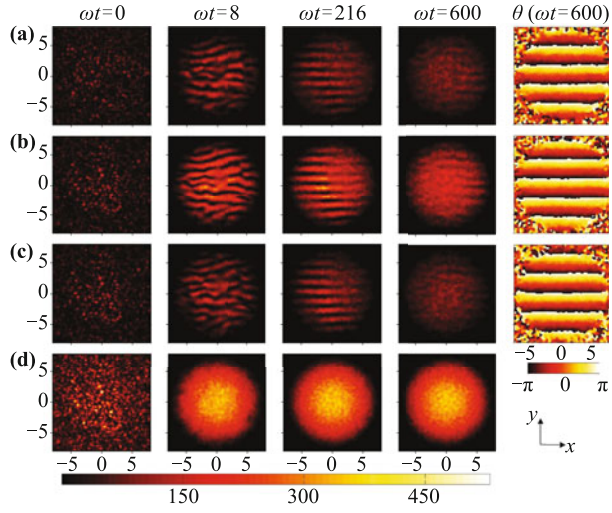

Fig. 13 Snapshots of the density profiles, **(a)** $|\psi_{-1}|^2$, **(b)** $|\psi_0|^2$, **(c)** $|\psi_1|^2$ and **(d)** total density of spin-1 BEC of ^{87}Rb during quench. The strengths of the spin–orbit coupling are $\kappa_x = 1$, $\kappa_y = 2$ and the final temperature is $k_BT = 2$. The axes of directions are indicated in the bottom right corner. The rightmost column shows the phase profile of equilibrium state. The final particle numbers are $N_{\pm1} \approx 7.44 \times 10^3$, $N_0 \approx 1.45 \times 10^4$. Reproduced from Ref. [106], Copyright © 2012 American Physical Society.

equilibrium state is in the plane wave phase [67]. In this case, spin domains appear shortly after the quench starts and arrays of spin vortices serve as the domain walls. As the system is approaching to the equilibrium state, the domain walls are expelled outward and finally disappear. The plane wave state is stable despite of finite fluctuations in the density and spin textures. The equilibrium state favors the plane wave phase if $\kappa_x \neq \kappa_y$ or $\kappa_x = \kappa_y = \kappa < 0.8$. If $\kappa_x = \kappa_y = \kappa > 0.8$, periodic structures composed of grids of dark solitons in $\psi_{\pm 1}$ components and vortices lattice in the ψ_0 component would appear. Corresponding to this density configuration, the spin texture consists of two interlacing square lattices of spin vortex with opposite vorticities, which we denote as the spin vortex lattice. For $\kappa > 0.8$, the equilibrium state will end up in the plane wave phase or the spin vortex lattice phase. However, when $\kappa > 4$ is satisfied, the equilibrium chooses the plane wave state.

The energy of the spin vortex lattice is numerically found greater than that of the plane wave phase. All the spin vortices in the spin vortex lattice exhibit similar structure: The central spin points to the z axis, and the others increasingly tilt outward and lie on the xy plane at the boundary. This is actually the Mermin–Ho vortex [16, 120, 121], or meron. A meron and its neighboring counterpart will pair up to form vortex-dipole to lower the total energy because of the ferromagnetic nature of the condensate. In addition, the density distribution of the spin vortex lattice state in the momentum space is characterized by four sharp peaks, showing the state is composed of four plane waves.

Next, we consider the spin–orbit coupled spinor BEC of ^{23}Na with the same parameter setting as that in the above explorations of the spinor BEC of ^{87}Rb. The numerical calculations show that there is no spin texture if the polar spin-1 gas is unpolarized initially. However, if the spin-1 gas is polarized, spin textures appears. Figure 14 shows the equilibrium spin texture for this spin-polarized state with a polarization ratio $M/N = 0.87$ (M is the total magnetic momentum).

Compared to that of a meron, the spin texture in Fig. 14(a) is arranged in a quite different manner. The spins in the boundary always point to z direction. Meanwhile, the inner ones tilt gradually and eventually lie on the xy plane. The topological charge of such a configuration is $Q = -1/2$. In Fig. 14(c) and (d), there are three inverted merons with distorted cores. However, The spin configuration with only one inverted [shown in Fig. 14(a) and (b)] has an lower energy than that with three inverted meroms. Actually, we find the isolated inverted meron is robust against the thermal fluctuations. Thus, we conclude that crystallization of merons are expected to be emerge in the ferromagnetic spinor BEC. On the other hand, isolated inverted merons can be generated in the initially polarized polar spinor BECs, such as the spin-1 BEC of ^{23}Na.

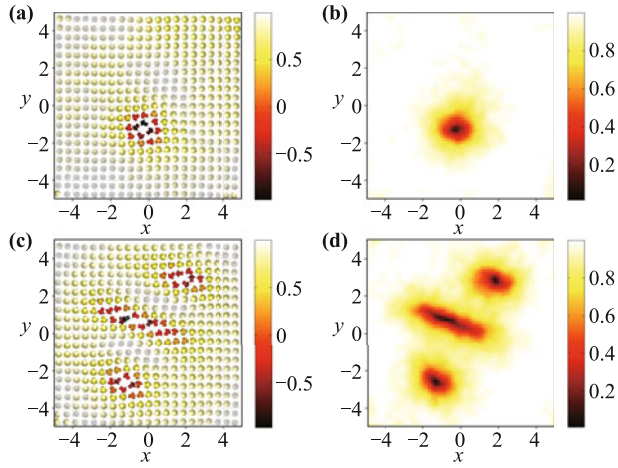

Fig. 14 **(a)**, **(c)** The spin texture in equilibrium and **(b)**, **(d)** the corresponding spin density distribution of the spin-1 BEC of ^{23}Na at $k_BT = 2$. The results for a single inverted meron are shown in (a) and (b), while those for the three inverted merons are shown in (c) and (d). The final particle numbers are $N_1 \approx 8.32 \times 10^4$, $N_0 \approx 1.95 \times 10^4$ and $N_{-1} \approx 82.21 \times 10^3$. Reproduced from Ref. [106], Copyright © 2012 American Physical Society.

In fact, half-skyrmion excitation depends on the combination of spin–orbit coupling and rotation. As found in Ref. [107], the half-skyrmions in this case originates from a dipole structure of spin which is always embedded in three vortices constructed by each condensate component, respectively. In the rotating spin–orbit coupled spin-1 BECs, the half-skyrmion (meron) can appear without pairing. For the half-skyrmion lattice in rotating spin-1 BEC, the numerical results is different from the periodic vortex lattice in Ref. [27] or the the vortices trimers in Ref. [33]. Instead, the vortices encircle the center with several circles.

In Fig. 15, we show the spin texture and the topological charge density in the spinor BEC of ^{87}Rb. It is shown that there are many half-skyrmions rounding the center. The topological charge density varies between -1 and 0, indicating that our results in Fig. 15(a) are half-skyrmions but not meron-antimeron pairs. We conclude that the half-skyrmions (meron) can occur but do not in the form of the meron-antimeron pairs.

6 Conclusions

In summary, we have investigated both the static and dynamic matter wave structures in spin-1 BECs. The ground state of the spin-orbit coupled spinor condensate is investigated in the presence of the external Zeeman field. By using the cavity quantum electrodynamics

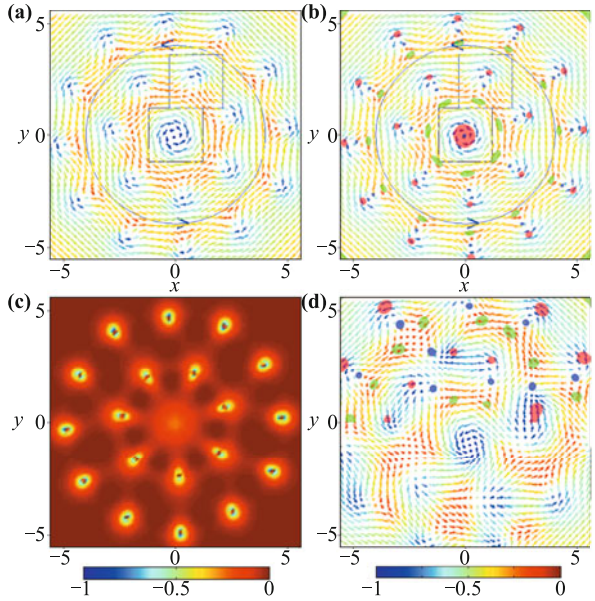

Fig. 15 **(a)** Spin texture of spinor BEC of ^{87}Rb with $\kappa = 0.5$ and $\Omega_r = 0.5\omega$. The color of each arrow indicates the magnitude of $\mathcal{F}_z$. The black pane points out a Skyrmion, and the blue pane indicates a half-Skyrmion. The blue arrows show the main direction of the spin texture. **(b)** The position of vortices and the spin texture. The green, blue and red spots are the center of vortices formed by the $m_F = -1$, $m_F = 0$ and $m_F = +1$ components, respectively. **(c)** Topological charge density. **(d)** The position of vortices and the spin texture of spinor BEC of ^{87}Rb with $\kappa = 0.1$ and $\Omega_r = 0.5\omega$. Noting, we only mark the vortices in $y > 0$ region in order to illuminate the spin texture and position of vortices clearly. The units of length and strength of spin–orbit coupling are $\sqrt{\frac{\hbar}{m\omega}}$, $\sqrt{\hbar\omega/m}$, respectively. Reproduced from Ref. [107], Copyright © 2012 American Physical Society.

techniques, the ferromagnetic and polar quantum ground states are possible to be distinguished. For the polar state, the intracavity photon number (as a function of detuning) is simple Lorentzian distribution; for the ferromagnetic ground states, however, the center and width of the curve vary widely depending on the inclination angle. Many kinds of soliton solutions of the one dimensional spin-1 condensate are found, and their stability is analyzed. Two dimensional ring dark solitons are studied, and they are found live longer lifetimes than that in the scalar BECs. In addition, the ring dark soliton in one component of the condensate inclines to induce ring dark solitons in other components, forming into long lived coexistence structures, which show quasi-periodic oscillations. Skyrmion lattices formed in rotating spin-1 BECs or spin–orbit coupled spinor BECs are investigated. It is predicted that crystallization of skyrmions and merons will arise in the spinor BECs.

Acknowledgements We would like to express our sincere thanks to Zheng-Wei Xie, Lu Li and J. M. Zhang for their original works and figures. This work was supported by the NKBRSFC under Grants Nos. 2011CB921502, 2012CB821305, 2009CB930701, and 2010CB922904, the NSFC under Grants Nos. 10934010, 11228409, 11247206, and 61227902, and the NSFC-RGC under Grants Nos. 11061160490 and 1386-N-HKU748/10.

References

1. D. M. Stamper-Kurn, M. R. Andrews, A. P. Chikkatur, S. Inouye, H. J. Miesner, J. Stenger, and W. Ketterle, Phys. Rev. Lett., 1998, 80(10): 2027
2. T. Ohmi and K. Machida, J. Phys. Soc. Jpn., 1998, 67(6): 1822
3. T. L. Ho, Phys. Rev. Lett., 1998, 81(4): 742
4. J. Stenger, S. Inouye, D. M. Stamper-Kurn, H. J. Miesner, A. P. Chikkatur, and W. Ketterle, Nature, 1998, 396(6709): 345
5. C. K. Law, H. Pu, and N. P. Bigelow, Phys. Rev. Lett., 1998, 81(24): 5257
6. M. Koashi and M. Ueda, Phys. Rev. Lett., 2000, 84(6): 1066
7. T. L. Ho and L. Yin, Phys. Rev. Lett., 2000, 84(11): 2302
8. H. J. Miesner, D. M. Stamper-Kurn, J. Stenger, S. Inouye, A. P. Chikkatur, and W. Ketterle, Phys. Rev. Lett., 1999, 82(11): 2228
9. H. Pu, C. K. Law, S. Raghavan, J. H. Eberly, and N. P. Bigelow, Phys. Rev. A, 1999, 60(2): 1463
10. M. S. Chang, C. D. Hamley, M. D. Barrett, J. A. Sauer, K. M. Fortier, W. Zhang, L. You, and M. S. Chapman, Phys. Rev. Lett., 2004, 92(14): 140403
11. A. Widera, F. Gerbier, S. Fölling, T. Gericke, O. Mandel, and I. Bloch, New J. Phys., 2006, 8(8): 152
12. N. Klausen, J. Bohn, and C. Greene, Phys. Rev. A, 2001, 64(5): 053602
13. F. Zhou, Phys. Rev. Lett., 2001, 87(8): 080401
14. G. W. Semenoff and F. Zhou, Phys. Rev. Lett., 2007, 98(10): 100401
15. T. Isoshima, K. Machida, and T. Ohmi, J. Phys. Soc. Jpn., 2001, 70(6): 1604
16. T. Mizushima, K. Machida, and T. Kita, Phys. Rev. Lett., 2002, 89(3): 030401
17. U. Leonhardt and G. E. Volovik, JETP Lett., 2000, 72(2): 46
18. T. Isoshima and K. Machida, Phys. Rev. A, 2002, 66(2): 023602
19. T. Isoshima, K. Machida, and T. Ohmi, J. Phys. Soc. Jpn., 2001, 70(6): 1604
20. H. T. C. Stoof, E. Vliegen, and U. Al Khawaja, Phys. Rev. Lett., 2001, 87(12): 120407
21. J. Ruostekoski and J. R. Anglin, Phys. Rev. Lett., 2003, 91(19): 190402
22. J. Ieda, T. Miyakawa, and M. Wadati, Phys. Rev. Lett., 2004, 93(19): 194102

23. E. V. Doktorov, J. Wang, and J. Yang, Phys. Rev. A, 2008, 77(4): 043617
24. H. E. Nistazakis, D. J. Frantzeskakis, P. G. Kevrekidis, B. A. Malomed, and R. Carretero-González, Phys. Rev. A, 2008, 77(3): 033612
25. M. Ueda and Y. Kawaguchi, Phys. Rep., 2012, 520: 253
26. W. Z. Bao and Y. Z. Zhang, Methods Appl. Anal., 2010, 17: 049
27. A. S. Bradley, C. Gardiner, and M. Davis, Phys. Rev. A, 2008, 77(3): 033616
28. S. J. Rooney, A. S. Bradley, and P. B. Blakie, Phys. Rev. A, 2010, 81(2): 023630
29. S. J. Rooney, P. B. Blakie, B. P. Anderson, and A. S. Bradley, Phys. Rev. A, 2011, 84(2): 023637
30. A. Sinatra, C. Lobo, and Y. Castin, J. Phys. B, 2002, 35(17): 3599
31. C. W. Gardiner and P. Zoller, Phys. Rev. A, 1998, 58(1): 1050
32. C. W. Gardiner and P. Zoller, Phys. Rev. A, 2000, 61(3): 033601
33. S. W. Su, C. H. Hsueh, I. K. Liu, T. L. Horng, Y. C. Tsai, S. C. Gou, and W. M. Liu, Phys. Rev. A, 2011, 84(2): 023601
34. Y. Hao, Y. Zhang, J. Q. Liang, and S. Chen, Phys. Rev. A, 2006, 73(5): 053605
35. L. Li, Z. Li, B. A. Malomed, D. Mihalache, and W. M. Liu, Phys. Rev. A, 2005, 72(3): 033611
36. N. P. Robins, W. Zhang, E. A. Ostrovskaya, and Y. S. Kivshar, Phys. Rev. A, 2001, 64(2): 021601
37. W. Zhang, D. L. Zhou, M. S. Chang, M. S. Chapman, and L. You, Phys. Rev. Lett., 2005, 95(18): 180403
38. H. Saito, Y. Kawaguchi, and M. Ueda, Phys. Rev. Lett., 2006, 96(6): 065302
39. S. Murakami, N. Nagaosa, and S. C. Zhang, Phys. Rev. B, 2004, 69(23): 235206
40. Y. J. Lin, R. L. Compton, A. R. Perry, W. D. Phillips, J. V. Porto, and I. B. Spielman, Phys. Rev. Lett., 2009, 102(13): 130401
41. Y. J. Lin, R. L. Compton, K. Jiménez-García, W. D. Phillips, J. V. Porto, and I. B. Spielman, Nat. Phys., 2011, 7(7): 531
42. Y. J. Lin, K. Jiménez-García, and I. B. Spielman, Nature, 2011, 471(7336): 83
43. M. Aidelsburger, M. Atala, S. Nascimbene, S. Trotzky, Y. A. Chen, and I. Bloch, Phys. Rev. Lett., 2011, 107(25): 255301
44. Z. Fu, P. Wang, S. Chai, L. Huang, and J. Zhang, Phys. Rev. A, 2011, 84(4): 043609
45. D. L. Campbell, G. Juzeliūnas, and I. B. Spielman, Phys. Rev. A, 2011, 84(2): 025602
46. T. D. Stanescu, B. Anderson, and V. Galitski, Phys. Rev. A, 2008, 78(2): 023616
47. S. Gopalakrishnan, A. Lamacraft, and P. M. Goldbart, Phys. Rev. A, 2011, 84(6): 061604
48. S. Sinha, R. Nath, and L. Santos, Phys. Rev. Lett., 2011, 107(27): 270401
49. H. Hu, B. Ramachandhran, H. Pu, and X. J. Liu, Phys. Rev. Lett., 2012, 108(1): 010402
50. J. Radić, T. A. Sedrakyan, I. B. Spielman, and V. Galitski, Phys. Rev. A, 2011, 84(6): 063604
51. H. Hu and X. J. Liu, Phys. Rev. A, 2012, 85(1): 013619
52. D. W. Zhang, Z. Y. Xue, H. Yan, Z. D. Wang, and S. L. Zhu, Phys. Rev. A, 2012, 85(1): 013628
53. B. Ramachandhran, B. Opanchuk, X. J. Liu, H. Pu, P. D. Drummond, and H. Hu, Phys. Rev. A, 2012, 85(2): 023606
54. R. Barnett, S. Powell, T. Grass, M. Lewenstein, and S. Das-Sarma, Phys. Rev. A, 2012, 85(2): 023615
55. W. Zheng and Z. B. Li, Phys. Rev. A, 2012, 85(5): 053607
56. C. M. Jian and H. Zhai, Phys. Rev. B, 2011, 84(6): 060508
57. Y. X. Du, H. Yan, D. W. Zhang, C. J. Shan, and S. L. Zhu, Phys. Rev. A, 2012, 85(4): 043619
58. M. Merkl, A. Jacob, F. E. Zimmer, P. Öhberg, and L. Santos, Phys. Rev. Lett., 2010, 104(7): 073603
59. Y. P. Zhang, L. Mao, and C. W. Zhang, Phys. Rev. Lett., 2012, 108(3): 035302
60. Y. Deng, J. Cheng, H. Jing, C. P. Sun, and S. Yi, Phys. Rev. Lett., 2012, 108(12): 125301
61. X. Q. Xu and J. H. Han, Phys. Rev. Lett., 2011, 107(20): 200401
62. X. F. Zhou, J. Zhou, and C. J. Wu, Phys. Rev. A, 2011, 84(6): 063624
63. Z. F. Xu, R. Lü, and L. You, Phys. Rev. A, 2011, 83(5): 053602
64. P. Wang, Z. Q. Yu, Z. Fu, J. Miao, L. Huang, S. Chai, H. Zhai, and J. Zhang, Phys. Rev. Lett., 2012, 109(9): 095301
65. G. Juzeliūnas, J. Ruseckas, and J. Dalibard, Phys. Rev. A, 2010, 81(5): 053403
66. T. L. Ho and S. Z. Zhang, Phys. Rev. Lett., 2011, 107(15): 150403
67. C. J. Wang, C. Gao, C. M. Jian, and H. Zhai, Phys. Rev. Lett., 2010, 105(16): 160403
68. S. K. Yip, Phys. Rev. A, 2011, 83(4): 043616
69. M. S. Chang, Q. S. Qin, W. X. Zhang, L. You, and M. S. Chapman, Nat. Phys., 2005, 1(2): 111
70. K. Murata, H. Saito, and M. Ueda, Phys. Rev. A, 2007, 75(1): 013607
71. L. Wen, Q. Sun, H. Q. Wang, A. C. Ji, and W. M. Liu, Phys. Rev. A, 2012, 86(4): 043602
72. I. B. Mekhov, C. Maschler, and H. Ritsch, Nat. Phys., 2007, 3(5): 319
73. S. Ashhab and A. J. Leggett, Phys. Rev. A, 2002, 65(2): 023604

74. F. Brennecke, T. Donner, S. Ritter, T. Bourdel, M. Köhl, and T. Esslinger, Nature, 2007, 450(7167): 268
75. Y. Colombe, T. Steinmetz, G. Dubois, F. Linke, D. Hunger, and J. Reichel, Nature, 2007, 450(7167): 272
76. J. M. Zhang, S. Cui, H. Jing, D. L. Zhou, and W. M. Liu, Phys. Rev. A, 2009, 80(4): 043623
77. J. Kronjäger, C. Becker, P. Navez, K. Bongs, and K. Sengstock, Phys. Rev. Lett., 2006, 97(11): 110404
78. Z. W. Xie, W. Zhang, S. T. Chui, and W. M. Liu, Phys. Rev. A, 2004, 69(5): 053609
79. H. Pu, W. P. Zhang, and P. Meystre, Phys. Rev. Lett., 2001, 87(14): 140405
80. K. Cross, C. P. Search, H. Pu, W. P. Zhang, and P. Meystre, Phys. Rev. Lett., 2002, 88: 033603
81. W. Zhang, H. Pu, C. P. Search, and P. Meystre, Phys. Rev. Lett., 2002, 88(6): 060401
82. D. I. Pushkarov and Kh. I. Pushkarov, Phys. Lett. A, 1977, 61(5): 339
83. V. V. Konotop, M. Salerno, and S. Takeno, Phys. Rev. E, 1997, 56(6): 7240
84. T. Bergeman, M. G. Moore, and M. Olshanii, Phys. Rev. Lett., 2003, 91(16): 163201
85. M. Olshanii, Phys. Rev. Lett., 1998, 81(5): 938
86. C. Becker, S. Stellmer, P. Soltan-Panahi, S. Dörscher, M. Baumert, E. Richter, J. Kronjäger, K. Bongs, and K. Sengstock, Nat. Phys., 2008, 4(6): 496
87. A. Weller, J. P. Ronzheimer, C. Gross, J. Esteve, M. K. Oberthaler, G. Theocharis, and P. G. Kevrekidis, Phys. Rev. Lett., 2008, 101(13): 130401
88. G. X. Huang, V. A. Makarov, and M. G. Velarde, Phys. Rev. A, 2003, 67(2): 023604
89. Y. S. Kivshar and X. Yang, Phys. Rev. E, 1994, 50(1): R40
90. H. E. Nistazakis, D. J. Frantzeskakis, B. A. Malomed, and P. G. Kevrekidis, Phys. Lett. A, 2001, 285(3–4): 157
91. A. Dreischuh, D. Neshev, G. G. Paulus, F. Grasbon, and H. Walther, Phys. Rev. E, 2002, 66(6): 066611
92. S. W. Song, D. S. Wang, H. Wang, and W. M. Liu, Phys. Rev. A, 2012, 85(6): 063617
93. L. Dobrek, M. Gajda, M. Lewenstein, K. Sengstock, G. Birkl, and W. Ertmer, Phys. Rev. A, 1999, 60(5): R3381
94. J. Denschlag, J. E. Simsarian, D. L. Feder, C. W. Clark, L. A. Collins, J. Cubizolles, L. Deng, E. W. Hagley, K. Helmerson, W. P. Reinhardt, S. L. Rolston, B. I. Schneider, and W. D. Phillips, Science, 2000, 287(5450): 97
95. Z. Dutton, M. Budde, C. Slowe, and L. V. Hau, Science, 2001, 293(5530): 663
96. N. S. Ginsberg, J. Brand, and L. V. Hau, Phys. Rev. Lett., 2005, 94(4): 040403
97. I. Shomroni, E. Lahoud, S. Levy, and J. Steinhauer, Nat. Phys., 2009, 5(3): 193
98. K. C. Wright, L. S. Leslie, A. Hansen, and N. P. Bigelow, Phys. Rev. Lett., 2009, 102(3): 030405
99. X. H. Hu, X. F. Zhang, D. Zhao, H. G. Luo, and W. M. Liu, Phys. Rev. A, 2009, 79(2): 023619
100. G. Theocharis, D. J. Frantzeskakis, P. G. Kevrekidis, B. A. Malomed, and Y. S. Kivshar, Phys. Rev. Lett., 2003, 90(12): 120403
101. X. F. Zhang, X. H. Hu, D. S. Wang, X. X. Liu, and W. M. Liu, Front. Phys., 2011, 6(1): 46
102. V. V. Konotop and L. Pitaevskii, Phys. Rev. Lett., 2004, 93(24): 240403
103. L. P. Pitaevskii and E. M. Lifshitz, Statistical Physics (part 2), 3rd Ed., Oxford: Pergamon, 1980, section 29
104. S. Inouye, M. Andrews, J. Stenger, H. Miesner, D. Stamper-Kurn, and W. Ketterle, Nature, 1998, 392: 151
105. C. Chin, R. Grimm, P. Julienne, and E. Tiesinga, Rev. Mod. Phys., 1998, 70: 1003
106. S. W. Su, I. K. Liu, Y. C. Tsai, W. M. Liu, and S. C. Gou, Phys. Rev. A, 2012, 86(2): 023601
107. C. F. Liu and W. M. Liu, Phys. Rev. A, 2012, 86(3): 033602
108. A. Y. Cherny, J. S. Caux, and J. Brand, Front. Phys., 2012, 7(1): 54
109. T. L. Horng, C. H. Hsueh, S. W. Su, Y. M. Kao, and S. C. Gou, Phys. Rev. A, 2009, 80(2): 023618
110. U. K. Rößler, A. N. Bogdanov, and C. Pfleiderer, Nature, 2006, 442(7104): 797
111. S. Mühlbauer, B. Binz, F. Jonietz, C. Pfleiderer, A. Rosch, A. Neubauer, R. Georgii, and P. Boni, Science, 2009, 323(5916): 915
112. X. Z. Yu, Y. Onose, N. Kanazawa, J. H. Park, J. H. Han, Y. Matsui, N. Nagaosa, and Y. Tokura, Nature, 2010, 465(7300): 901
113. D. A. Ivanov, Phys. Rev. Lett., 2001, 86(2): 268
114. A. Actor, Rev. Mod. Phys., 1979, 51(3): 461
115. L. Brey, H. A. Fertig, R. Cote, and A. H. MacDonald, Phys. Rev. B, 1996, 54(23): 16888
116. G. E. Brown and M. Rho, The Multifaced Skyrmion, Singapore: World Scientific, 2010
117. V. M. H. Ruutu, J. Kopu, M. Krusius, U. Parts, B. Placais, E. V. Thuneberg, and W. Xu, Phys. Rev. Lett., 1997, 79(25): 5058
118. R. Ishiguro, O. Ishikawa, M. Yamashita, Y. Sasaki, K. Fukuda, M. Kubota, H. Ishimoto, R. Packard, T. Takagi, T. Ohmi, and T. Mizusaki, Phys. Rev. Lett., 2004, 93(12): 125301
119. A. E. Leanhardt, Y. Shin, D. Kielpinski, D. E. Pritchard, and W. Ketterle, Phys. Rev. Lett., 2003, 90(14): 140403
120. T. Mizushima, K. Machida, and T. Kita, Phys. Rev. A, 2002, 66(5): 053610
121. T. Kita, T. Mizushima, and K. Machida, Phys. Rev. A, 2002, 66: 061601(R)